Geophys. J. Int. (2001) **147,** 639–659

Effects of vertical boundaries on infinite Prandtl number thermal convection

Jun Korenaga[1,*] and Thomas H. Jordan[2]

[1] *Department of Earth, Atmospheric, and Planetary Sciences, Massachusetts Institute of Technology, Cambridge, USA*
[2] *Department of Earth Sciences, University of Southern California, Los Angeles, USA*

Accepted 2001 July 30. Received 2001 July 12; in original form 2001 March 5

SUMMARY

The physics of thermomechanical coupling of the continental lithosphere and its surrounding mantle is studied using a simple hydrodynamic model in which a fluid is heated from below and is bounded by rigid side walls. Rayleigh numbers up to 10^6 are considered. A series of finite-element stability analyses is employed to characterize systematically the nature of convective instability in such a system. The marginal stability of a bounded fluid is increased not only by the rigid boundary condition on side walls, but also by heat conduction across side walls. The planform of convection at the marginal state is 3-D, having convective rolls aligned perpendicular to side walls. The characteristics of non-linear convection at supercritical Rayleigh numbers are investigated by first calculating 2-D steady-state solutions and then applying 2-D and 3-D stability analyses. The 2-D stability analysis shows that the presence of side walls significantly reduces the transition Rayleigh number for time-dependent convection, and the 3-D stability analysis shows that heat conduction through side walls strongly prefers 3-D convective motion. Finally, the characteristics of 3-D convection are analysed through the 3-D single-mode approximation. Both 2-D and 3-D single-mode solutions demonstrate that conducting side walls reduce the strength of convection at low Rayleigh numbers but have a negligible influence at higher Rayleigh numbers. We therefore propose that the basal topography of the continental lithosphere can modulate the convective planform efficiently in the upper mantle.

Key words: lithosphere, mantle convection, upper mantle.

1 INTRODUCTION

Multiple spatial and temporal scales are inferred for mantle convection, such as: (1) global-scale flow represented by plate tectonics (e.g. Hager & O'Connell 1981; Bunge *et al.* 1998); (2) thermal plumes originating in boundary layer instabilities at the core–mantle boundary (e.g. Whitehead 1988); and (3) small-scale convection in the upper mantle driven by surface cooling (e.g. Richter 1973b; Solomatov & Moresi 2000). Mantle convection is considered to be the fundamental cause for a number of geological phenomena. In particular, decompressional mantle melting associated with convective upwelling is the major source of magmatic activities on the Earth. Understanding the pattern of multiscale convection is thus intimately related to resolving the driving mechanism of terrestrial magmatism. Our primary interest in this paper is to understand the nature of small-scale convection and its relevance to top boundary conditions imposed by geological structure such as continent–ocean heterogeneity.

The thickness of the Earth's lithosphere (used as a cold and mechanically strong surface layer throughout this paper) varies significantly on a global scale, especially in association with the continental lithosphere, as inferred from global seismic tomography (e.g. Montagner & Tanimoto 1991; Zhang & Tanimoto 1993; Su *et al.* 1994; Ritzwoller & Lavely 1995), as well as regional seismic studies (e.g. Jordan 1988; Grand 1994; Gaherty & Jordan 1995; Simons *et al.* 1999), and a change in lithospheric thickness of as large as 200 km is common at continent–ocean boundaries. Characterizing sublithospheric convection with such a variable thickness of lithosphere is important in understanding how near-surface structure can interact with mantle convection (e.g. Anderson 1998a). A strong spatial association between continental margins and flood basalts, for example, led Anderson (1994) to suggest that the lithosphere plays the

* Now at: Department of Earth and Planetary Science, University of California, Berkeley, USA. .E-mail: korenaga@seismo.berkeley.edu

principal role in the dynamics of exceptionally voluminous volcanism, as opposed to a more common explanation based on deep-seated mantle plumes (e.g. Richards *et al.* 1989; White & McKenzie 1989; Hill *et al.* 1992). Compared with mantle plumes, however, the importance of a heterogeneous top boundary on mantle convection has attracted less attention, and the number of geodynamical studies into this problem has been limited.

The main objective of this paper is to derive scaling laws that will be useful in assessing how the characteristics of mantle convection can be affected by the structure of the top boundary, on the basis of steady-state solutions. The thick continental lithosphere has both thermal and kinematic effects on small-scale convection in the adjacent asthenospheric mantle. We will study the influence of vertical boundaries on a convecting fluid, to understand the essence of the strongly varying basal topography of the lithosphere on the underlying mantle convection. A simple hydrodynamic model of a fluid with both horizontal and vertical rigid boundaries will be analysed systematically using a series of stability analyses and will be characterized by several scaling laws such as the Rayleigh number–Nusselt number relationship. After reviewing previous studies regarding heterogeneous boundary conditions in Section 2, our model configuration is described in detail in Section 3. The effects of side walls on marginal stability are studied using the variational method in Section 4. The characteristics of 2-D finite-amplitude convection at supercritical Rayleigh numbers are then investigated using perturbation analyses in Section 5. The effects of three-dimensionality on finite-amplitude convection is investigated in Section 6, where the 3-D single-mode approximation is introduced. Finally, the relevance of our study to mantle dynamics and terrestrial magmatism is discussed in Section 7.

2 PREVIOUS STUDIES

A few authors have considered the influence of a variable lithospheric thickness through a perturbation approach (Busse 1978; Zhang & Busse 1997), but this type of treatment is limited to a small amplitude of thickness variation with respect to the vertical scale of a convective system. Although the Earth's mantle has a depth extent of about 3000 km, a proper vertical scale for the convective interaction with near-surface structure may be that of the upper mantle. The mantle viscosity structure is very likely to be layered, the lower mantle being more viscous than the upper mantle (Hager *et al.* 1985; Forte & Mitrovica 1996; Simons & Hager 1997), and an endothermic phase transition at the base of the upper mantle may retard material flux (Honda *et al.* 1993; Tackley *et al.* 1993; Solheim & Peltier 1994; Tackley 1995). Although it is now widely perceived that neither the layered viscosity structure nor the endothermic phase change is sufficient to completely isolate the convection system of the upper mantle from that of the lower mantle with regard to global-scale mantle circulation, one should still recognize that they can significantly influence convective motion with short wavelengths. Convection beneath the lithosphere driven by surface cooling [also known as 'rigid-lid convection' (Solomatov 1995)] is indeed characterized by short-wavelength structure (e.g. Davaille & Jaupart 1993). In this paper we will focus on this type of 'small-scale' convection in the upper mantle (that is, with a length scale smaller than 500 km); one should not confuse this with global-scale upper-mantle convection isolated from the lower mantle (e.g. Richter & McKenzie 1981), which now seems to be unlikely on the basis of recent seismic tomography studies (e.g. van der Hilst *et al.* 1997).

For such small-scale convection, the thickness variation of the lithosphere (such as the variations expected at continent–ocean transitions) would exceed the valid range of linear approximations in the perturbation analyses. The influence of a sharp spatial variation in boundaries on a convective system is a highly non-linear problem. It has been considered with some specific model geometries, such as for convection due to slab cooling (Rabinowicz *et al.* 1980; Nataf *et al.* 1981; Christensen 1983) and for convection due to cratonic lithosphere or rifting-generated lithospheric necking (e.g. Richter 1973a; Elder 1976; Mutter *et al.* 1988; Keen & Boutilier 1995; King & Anderson 1998). Because these studies focus on specific geological problems, it is difficult to extract the general effects of a heterogeneous top boundary. Moreover, an initial-value approach is common in these convection studies (Mutter *et al.* 1988; Keen & Boutilier 1995; Boutilier & Keen 1999), so their results depend critically on a particular choice of initial conditions.

3 MODEL CONFIGURATION

Because our approach to the investigation of the influence of the continental lithosphere is very different from previous ones, and also because for some readers it may not be clear how our model configuration is relevant to the actual mantle system, a detailed explanation as well as justification are given below.

The geometry of the model boundaries is 2-D. As shown in Fig. 1, while a fluid is bounded laterally in one of the horizontal coordinates (x, hereafter called the in-plane coordinate), its extent is infinite in the other horizontal coordinate (y, the out-of-plane coordinate). This model configuration is motivated by the fact that a stepwise change in lithospheric thickness associated with a continent–ocean transition can be reasonably approximated as a linear feature for the scale of upper-mantle convection. A fluid is heated from below, that is, the surface and the bottom temperature are fixed at zero and some positive temperature, ΔT, respectively. Convective motions in such systems are not necessarily 2-D, and we will investigate both 2-D and 3-D cases. The aspect ratio of the model domain, r, is defined as the width of the domain divided by its depth, and several different aspect ratios will be considered.

The side walls have both kinematic and thermal effects on convection, through their mechanical and thermal boundary conditions. In all cases, all boundaries are rigid (i.e. no slip). Two different thermal boundary conditions, i.e. 'conducting' and insulating, are applied to the side walls to determine their contrasting effects. For the 'conducting' side walls, a linear temperature profile is imposed along the side walls. A linear profile (as opposed to any other temperature variation) is chosen to preserve the top–bottom symmetry of the system. For the same reason, a rigid lower boundary is assumed, though this may also be justified by the possible jump in viscosity at the base of the upper mantle.

The mantle 'fluid' is assumed to have an infinite Prandtl number and uniform viscosity. We also employ the Boussinesq approximation to the conservation equations of mass and momentum, and use the finite-element method to solve viscous momentum equations and thermal advection–diffusion equations.

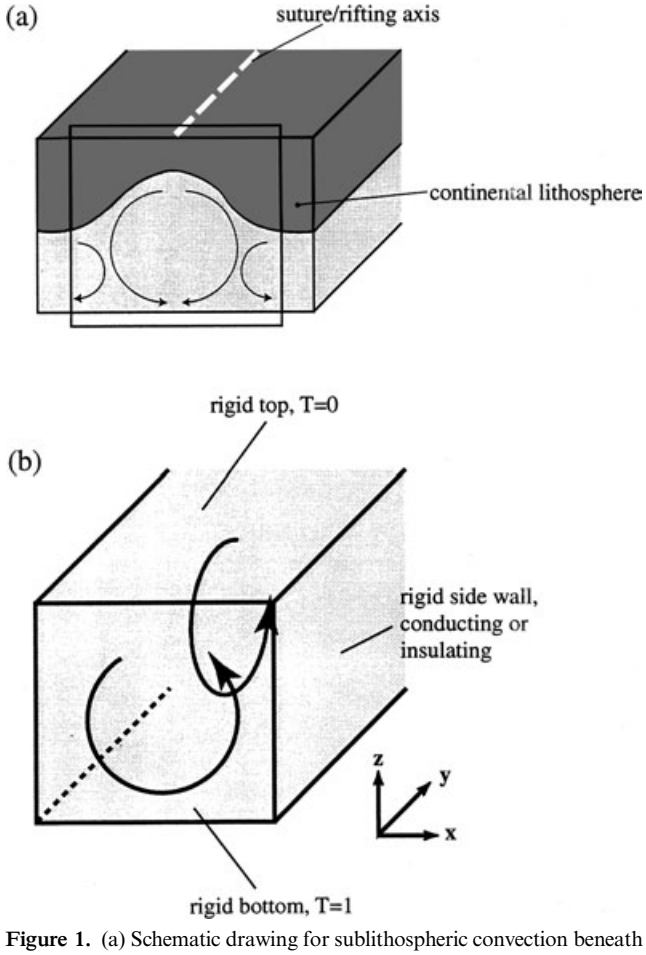

Figure 1. (a) Schematic drawing for sublithospheric convection beneath continental lithosphere with a variable thickness. A large variation in thickness with a relatively short wavelength may be expected beneath a suture zone, where asthenospheric mantle is bounded by adjacent thick cratonic lithosphere. (b) An idealized hydrodynamic model considered in this study, to investigate the nature of sublithospheric convection within a domain enclosed by a box in (a).

Though temperature dependence is important for the rheology of the upper mantle in general (e.g. Karato & Wu 1993), in this study we are concerned with the regime of rigid-lid convection (e.g. Solomatov 1995), which can be well described as being nearly isoviscous convection. The activation energy for temperature dependence is so high (>100 kJ mol^{-1}) that most of temperature variation is confined within a nearly rigid, top thermal boundary layer. The expected temperature variation associated with sublithospheric small-scale convection is probably not greater than 100 K, and the corresponding viscosity variation should be smaller than 10 (Davaille & Jaupart 1993). The use of uniform viscosity therefore does not invalidate the applicability of our study to small-scale convection in the Earth's mantle. With a temperature perturbation of 100 K and an asthenospheric viscosity of 10^{19}–10^{20} Pa s, the Rayleigh number for small-scale convection in the upper mantle is of the order of 10^5–10^6, so we will consider Rayleigh numbers up to 10^6. To resolve thermal boundary layers accurately, uniform 2-D quadrilateral elements with a non-dimensional size of 0.02×0.02 are used to discretize the model domain.

Convection stability of a fluid layer heated from below and cooled from above in a rectangular cylinder was studied by Velte (1964) for 2-D marginal stability with conducting side walls and by Frick & Clever (1982) for steady-state finite-amplitude convection with insulating side walls. Other than these, our solutions for finite-amplitude convection and corresponding stability analyses are a new contribution. We note that the rectangular geometry used in this paper has often been employed with a different thermal boundary condition (differential horizontal heating) to investigate the efficiency of convective heat transfer between two vertical walls at different temperatures (e.g. Ravi *et al.* 1994; Le Quere & Behnia 1998), which is a classical problem in fluid dynamics first studied by Batchelor (1954).

This model geometry has no direct analogue in the actual mantle convection system. We are interested in quantifying how *different* this system with side walls is from the classical model of an infinite horizontal layer, which can also be seen as a limiting case. By systematically characterizing the deviation from the classical model, we can generalize the influence of lithospheric side walls on small-scale convection. It is this deviation that we regard as being the most important. The virtue of our approach lies in its simplicity and comprehensiveness, not in an effort to simulate realistic complexity in mantle convection.

4 EFFECTS OF SIDE WALLS ON MARGINAL STABILITY

The equations for infinite-Prandtl-number thermal convection are governed by the Rayleigh number. The critical Rayleigh number corresponds to the onset of convection, and it plays a fundamental role in various scaling laws, such as the relationship between the Rayleigh number and the amplitude of convection (e.g. Chandrasekhar 1981). The critical Rayleigh number varies with different boundary conditions. A fluid bounded by rigid horizontal boundaries, for example, has a higher critical Rayleigh number ($\sim$1708) than that with free-slip boundaries ($\sim$657); a fluid becomes less prone to convect when a free-slip condition is replaced by a rigid condition. A similar argument can be made for the addition of vertical side walls to a convective system, and some increase in the critical Rayleigh number is expected. Since the separation of variables is impossible when a fluid is bounded by both rigid horizontal and vertical boundaries, we will employ the variational method to obtain approximate critical Rayleigh numbers (e.g. Davis 1967; Charlson & Sani 1971; Chen 1992).

4.1 Variational formulation

The non-dimensionalized first-order perturbation equations for the marginally stable state are:

(1) conservation of mass

$$\nabla \cdot \mathbf{u} = 0; \tag{1}$$

(2) conservation of momentum

$$-\nabla P + \nabla^2 \mathbf{u} - Ra\,\theta \mathbf{e}_z = 0; \tag{2}$$

(3) conservation of energy

$$w + \nabla^2 \theta = 0, \tag{3}$$

where **u** is the normalized velocity, w is its vertical component, P is the normalized pressure, $\mathbf{e}_z$ is a unit vector in the upward direction and θ is the temperature perturbation from a linear conductive thermal profile, normalized using ΔT. The spatial scale is normalized with a system height of d, and the velocity scale is normalized with κ/d, where κ is the thermal diffusivity. The Rayleigh number, Ra, is defined as

$$Ra = \frac{\alpha \rho_r g \Delta T d^3}{\kappa \mu}, \tag{4}$$

where α is the thermal expansivity, ρ_r is a reference density, g is the gravitational acceleration and μ is the viscosity. For some specific values of Ra, the governing equations with the boundary conditions given above allow a non-zero solution, and the critical Rayleigh number is the minimum of such a solution family such as

$$Ra_c = \min_{\theta,\hat{w}} \frac{\int_V \theta \nabla^2 \theta dV}{-\int_V \theta \hat{w} dV}, \tag{5}$$

where $\hat{w}$ is the vertical velocity field corresponding to the given temperature field, θ, with unit Rayleigh number. This is the temperature-based variational formulation for the marginally stable state (Chandrasekhar 1981). The use of a unit velocity field requires that all boundary conditions are homogeneous, which is satisfied by our model configuration.

Using a finite-dimensional approximation such as

$$\theta = \sum_{i=1}^{n} \beta_i \theta_i, \tag{6}$$

$$\hat{w} = \sum_{i=1}^{n} \beta_i \hat{w}_i, \tag{7}$$

where θ_i are trial functions, the variational statement leads to the following eigenvalue problem:

$$\mathbf{A}\boldsymbol{\beta} = \lambda \mathbf{D}\boldsymbol{\beta}, \tag{8}$$

where

$$A_{ij} = \int_V \theta_i \hat{w}_j dV, \tag{9}$$

$$D_{ii} = \int_V \theta_i \nabla^2 \theta_i dV, \tag{10}$$

$$\lambda = Ra^{-1}. \tag{11}$$

Both **A** and **D** are positive-definite, so all eigenvalues are real and positive. The critical Rayleigh number corresponds to the largest eigenvalue, λ_{max}. We choose the temperature trial functions, θ_i, as

$$\theta_i = \sin(p_i \pi x) \cos(\psi y) \sin(q_i \pi z) \tag{12}$$

for conducting side walls, and

$$\theta_i = \cos(p_i \pi x) \cos(\psi y) \sin(q_i \pi z) \tag{13}$$

for insulating side walls. p_i and q_i are non-negative integers and ψ is a real number. The smallest q_i is always unity. The smallest p_i is unity except for the case of 3-D stability with insulating side walls, for which the smallest p_i is zero. A velocity field corresponding to a temperature trial function is calculated using a finite-element solver for Stokes flow (e.g. Hughes 1987). Its root-mean-square error with our mesh discretization is expected to be less than 0.2 per cent (Moresi *et al.* 1996). Since the matrix **D** can be calculated analytically, only 2-D numerical integration is required to calculate the matrix **A**.

4.2 Results for 2-D perturbations

We use all possible trial functions with $\psi = 0$ and $p_i + q_i \leq N$, where N denotes the maximum mode of the finite-dimensional approximation. The variational solution is merely an upper bound for the true critical Rayleigh number, so that N must be increased until convergence is obtained. Convergence is defined here such that a relative change between solutions for N and $N+2$ does not exceed 0.1 per cent. Monotonic convergence is guaranteed in the variational method, and we found that $N < 10$ is usually sufficient (e.g. Fig. 2). A

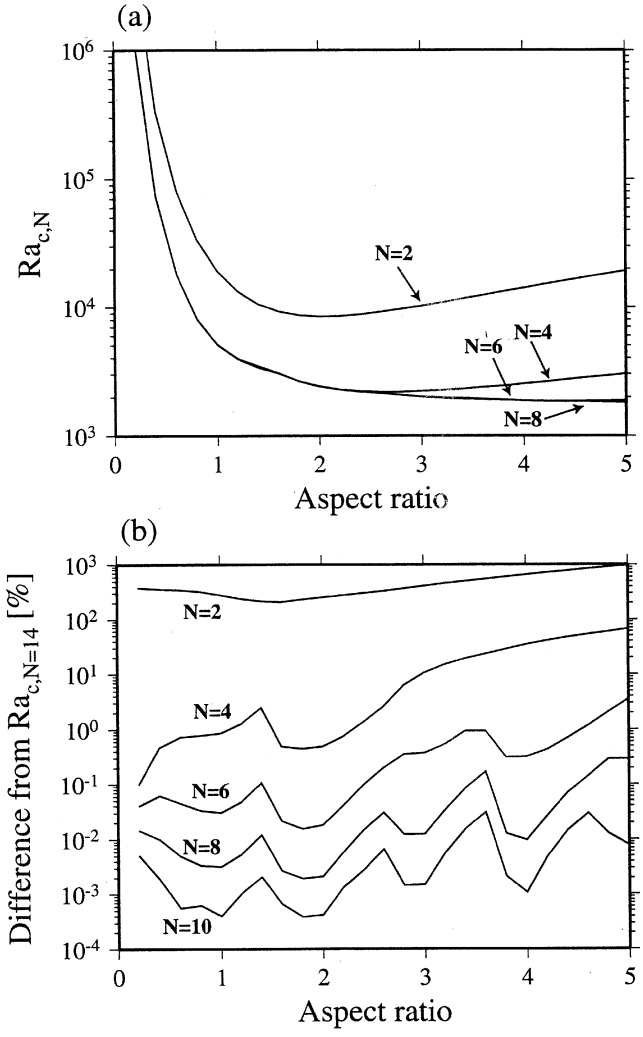

Figure 2. Example of convergence in the variational method. (a) Approximate critical Rayleigh numbers for 2-D perturbations with conducting side walls are shown for different numbers of modes. (b) Percentage differences from critical Rayleigh numbers calculated with $N = 14$ are shown for $N = 2$–10 as a function of the aspect ratio. Note that the differences are reduced by about an order of magnitude as the number of modes is increased by two. Solutions obtained with $N = 10$ have a less than 0.01 per cent difference for aspect ratios smaller than 3.

comparison with the critical Rayleigh numbers calculated by Velte (1964) for the conducting case shows a difference of about 0.5 per cent in general, which is consistent with the expected accuracy from our finite-element discretization. Since we are mainly interested in the first-order characteristics of stability curves for relatively small aspect ratios, this level of accuracy is sufficient.

The stability curves for 2-D perturbations are presented in Fig. 3(b) as a function of the aspect ratio, for insulating and conducting side walls. For conducting side walls, the critical Rayleigh number is 32 980, 5050 and 2397 at $r=0.5$, 1.0 and 2.0, respectively. The case with no side walls has a critical Rayleigh number of 1708 (at a wavelength of ~ 2; see Fig. 3a), so the influence of the side walls on marginal stability is almost insignificant for aspect ratios greater than 2. The divergent character of the stability curves for small aspect ratios is also evident in the stability curve for a layer of fluid with an infinite horizontal extent, if the latter is plotted as a function of a given perturbation wavelength (Fig. 3a). This indicates that the increase in the critical Rayleigh number for a narrower channel simply results from wavenumber selection imposed by a small aspect ratio. At a given aspect ratio, the critical Rayleigh number for conducting side walls is always larger than that for insulating side walls. Because the insulating boundary condition is a natural boundary condition, which is automatically satisfied in the variational formulation, the trial function space in the variation formulation associated with the insulating case is larger than that with the conducting case (Charlson & Sani 1970). Therefore, the critical Rayleigh number of the conducting case is always an upper bound for that of the insulating case. A more physical explanation may be given by considering the role of thermal diffusion in convection. Because conducting side walls enhance thermal diffusion compared with insulating ones, and because thermal diffusion tends to hinder convection, the critical Rayleigh number is larger for the cases with conducting side walls than those with insulating ones. The inflections in the stability curves, which are more clearly observed for the insulating case, correspond to changes in the number of convective rolls and indicate the composite nature of the stability curves (e.g. Davis 1967).

4.3 Results for 3-D perturbations

Because of the infinite horizontal extent in the out-of-plane coordinate, a general 3-D perturbation in the model can be decomposed into a sum of single-mode perturbations, each of which has a fixed out-of-plane wavenumber. 3-D Stokes flow generated by a single-mode perturbation in the temperature field can be calculated efficiently by 2-D finite-element procedures (see Appendix A). Stability curves as a function of the out-of-plane wavenumber were calculated for each value of the aspect ratio (Fig. 4a), and by taking the minimum of each stability curve, the final 3-D stability curve was constructed as a function of aspect ratio (Fig. 4b).

For the reason stated above regarding the relative size of function space, critical Rayleigh numbers for 3-D perturbations are always smaller than those for 2-D perturbations. The out-of-plane wavelength at which a stability curve takes the minimum is always finite, varying from ~ 1 to ~ 2 for aspect ratios between 0.25 and 2.0, showing that, in the most stable convective pattern, convective rolls are aligned perpendicular to side walls. Because of the increased degree of freedom allowed by out-of-plane convection, there should be a negligible influence of the in-plane wavenumber selection imposed by the aspect ratio. The calculated stability curves therefore reflect the effect of wall friction along the sides of convective rolls. It is interesting, therefore, that the most stable out-of-plane wavelength is close to 1 for aspect ratios of less than 0.5; a strong influence of wall friction seems to prevent otherwise stable cellular convection with a wavelength of ~ 2. Nonetheless, this wall friction has a much weaker influence on the critical Rayleigh number than the mode selection in the in-plane coordinate, as seen from a drastic decrease in the 3-D critical Rayleigh number at small aspect ratios.

5 2-D FINITE-AMPLITUDE CONVECTION IN A BOUNDED FLUID

For supercritical Rayleigh numbers, thermal convection becomes highly non-linear and generally time-dependent. One way to

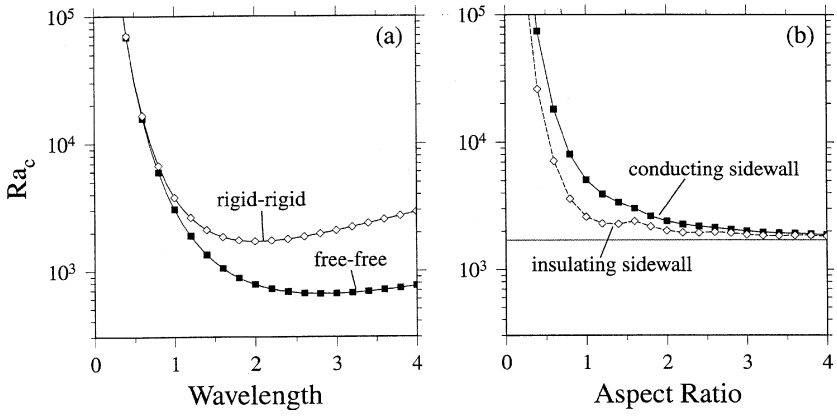

Figure 3. Critical Rayleigh numbers for 2-D perturbations. (a) Ra_c for the classical case with an infinite horizontal extent is plotted as a function of wavelength (solid lines). Overlaid symbols are solutions obtained by our variational method. (b) Ra_c for a fluid heated from below and bounded by 2-D rigid side walls is plotted as a function of model aspect ratio. Open diamonds denote variational solutions for insulating side walls, and solid squares for conducting side walls.

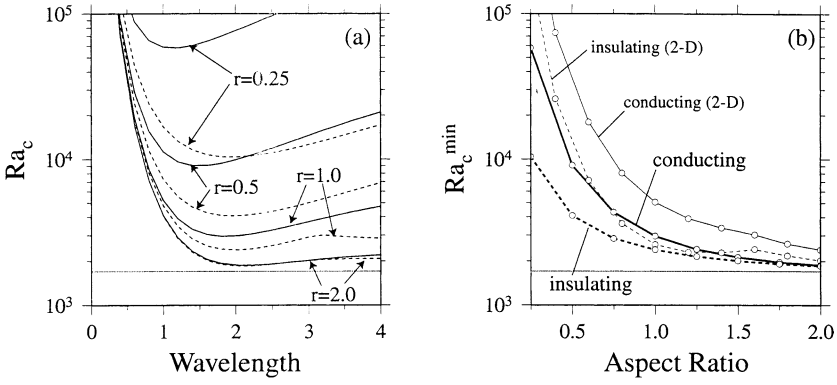

Figure 4. Critical Rayleigh number for 3-D perturbations. (a) Ra_c as a function of the out-of-plane wavelength, $2\pi/\psi$, is plotted for insulating (dashed) and conducting (solid) cases, at aspect ratios of 0.25–2.0. (b) Ra_c is plotted as a function of the aspect ratio. Thick solid and dashed lines are 3-D Ra_c for conducting and insulating cases, respectively. Also shown as thin curves are 2-D Ra_c. The grey horizontal line denotes Ra_c for the system with an infinite horizontal extent ($\sim$1708).

characterize such a convective system is to conduct fully time-dependent calculations and calculate some statistical measures from them. Alternatively, the characteristics of convection past marginal stability may be succinctly represented by those of steady-state solutions if they exist. We take the latter approach because steady-state solutions can be quickly obtained using the temperature under-relaxation method (Christensen 1984). A stability analysis is then applied to steady-state solutions, because they could be artificially stabilized by the relaxation method. This steady-state solution approach supplemented with a stability analysis provides a concise summary for the nature of supercritical convection, and it can efficiently determine a transition to time-dependent convection. Most of our analyses in this section are restricted to a purely 2-D framework. A 3-D stability analysis will be conducted at the end to test the validity of this 2-D assumption.

5.1 Perturbation analysis

With the Boussinesq approximation, the governing equations for the convective system with a supercritical Rayleigh number are comprised of: the equation of mass conservation, eq. (1); the equation of momentum conservation, which is the same as eq. (2) except that the perturbation temperature θ is replaced by the total temperature T; and the equation of energy conservation,

$$\frac{\partial T}{\partial t} + \mathbf{u}\cdot\nabla T = \nabla^2 T\,. \tag{14}$$

A temporal derivative appears only in the energy equation, so a steady-state solution can be obtained by dropping the first term of the left-hand side of eq. (14) *ab initio*, with an initial guess for a steady-state temperature field, and iterating between the Stokes flow equation and the modified energy equation until convergence is attained. A purely implicit method is used to solve the steady-state energy equation (e.g. Hughes 1987). Rapid convergence is possible by temperature under-relaxation during iterations (Christensen 1984). We start with an under-relaxation factor of 0.5, which is gradually increased whenever convergence is not obtained in given iterations. As a criterion for convergence, we use a root-mean-square difference of 0.05 per cent in the velocity fields of consecutive iterations.

Convergence obtained in the under-relaxation method does not necessarily mean that a resultant 'steady-state' solution is stable. If a high degree of under-relaxation is required for convergence, for example, it is generally the sign of an unstable solution. A solution is called stable if it can maintain its structure against any kind of perturbation. The stability of a steady-state solution can be tested by integrating the time-dependent energy equation (14) with an explicit time-stepping method (e.g. Christensen 1987; Hansen & Ebel 1988), or by a perturbation analysis described below (e.g. Busse 1967), which is more quantitative and complete.

Denoting steady-state temperature and velocity fields by T_0 and u_0, respectively, the energy equation for a perturbed state may be expressed to first order as

$$\frac{\partial \theta}{\partial t} = -\mathbf{u}_0\cdot\nabla\theta - \mathbf{u}\cdot\nabla\theta_0 + \nabla^2\theta\,, \tag{15}$$

where θ is the deviation from the steady-state temperature and $\mathbf{u}$ is the perturbation velocity field generated by θ (eq. 2). For a real steady-state solution, any kind of initial perturbation temperature must decay to null. Assuming an exponential time dependence for perturbation temperature such as $\theta\sim\exp(\sigma t)$, and using the same finite-dimensional approximation as in eqs (6) and (7), the above perturbation equation leads to the following eigenvalue problem:

$$\mathbf{A}\boldsymbol{\beta} = \sigma\mathbf{B}\boldsymbol{\beta}\,, \tag{16}$$

where

$$A_{ij} = \int_V [\theta_i\nabla^2\theta_j - \theta_i(\mathbf{u}_0\cdot\nabla)\theta_j - \theta_i(\mathbf{u}_j\cdot\nabla)\theta_0]dV\,, \tag{17}$$

$$B_{ii} = \int_V \theta_i^2 dV\,. \tag{18}$$

Although $\mathbf{B}$ is diagonal, $\mathbf{A}$ is non-symmetric, so eigenvalues are generally complex numbers. The maximum real part of the eigenvalues, which is called a growth exponent, determines the stability of the steady-state solution under consideration; a steady-state solution must have a negative growth exponent. The temperature trial functions are the same as eqs (12) and (13) except for the following: the smallest p_i is zero for both 2-D and 3-D stability with insulating side walls. Even though the trial functions with the form of eq. (13) do not generate

any velocity field in the 2-D framework for $p_i = 0$, the 2-D perturbation analysis must include the modes with $p_i = 0$ because of their coupling with the steady-state solution.

5.2 Stability for 2-D perturbations

Without any formal analysis, a qualitative understanding of stability may be obtained from the structure of a steady-state temperature field (Fig. 5). Whereas the rigid boundary condition on side walls does not strongly alter the temperature field, the influence of the conducting boundary condition is significant; the steady-state solution with a Rayleigh number of 10^5 for conducting side walls, for example, seems very unlikely to be stable. As in the variational formulation for the critical Rayleigh number, the number of trial functions used in the perturbation analysis must be increased until convergence is attained for a growth exponent. Because the perturbation equation is not self-adjoint, monotonic convergence is not guaranteed. Nevertheless, we found that a finite-dimensional approximation with $N/r = 10$–15 is usually sufficient for convergence.

Since the system of steady-state convection is non-linear, a steady-state solution is generally non-unique. For example, at least three different modes of a steady-state solution, i.e. one odd mode and two even modes (Fig. 6a), can be found by using an appropriate initial guess in the temperature under-relaxation method. The two even modes share the same stability curve owing to their symmetrical relation. Note that the dominant horizontal wavenumber for the even modes shown in Fig. 6 is 2π, whereas that for the odd mode is π. The odd mode is the fundamental mode in this case of $r = 1$. This explains the instability of the even-mode solutions for Ra less than 1.8×10^4. The stability of the even modes over the odd mode for Ra of 2.3×10^4–7×10^4 arises from the interaction with conducting side walls. In this range of Rayleigh numbers, the left–right symmetry in the imposed temperature profile on the side walls makes the even-mode solutions more stable. Despite these differences, the first-order behaviour of these growth exponents as a function of the Rayleigh number is similar, especially in the transition from a stable or moderately unstable regime to a very unstable regime (Fig. 6b). We chose to use the odd-mode solutions for $r = 0.5$ and 1.0 and the even-mode solutions for $r = 2.0$; that is, we tried to obtain steady-state convection cells with an aspect ratio close to unity. It is not always easy to obtain a solution with arbitrary symmetry because of our approach with the finite-element method, and the above strategy is based on the robustness of solutions in terms of the temperature relaxation method.

Growth exponents as a function of the Rayleigh number are shown in Fig. 7 for three different aspect ratios (0.5, 1.0 and 2.0) and for conducting and insulating boundary conditions. Also shown is the stability curve for the case of no side wall (i.e. a reflecting boundary condition at the sides) with a unit aspect ratio. Regardless of the type of thermal boundary condition on the side wall, the transition to an unstable regime is abrupt. The Rayleigh number that marks this transition to time-dependent solutions is sometimes called the critical Rayleigh number of the second kind (e.g. Busse 1967). The Rayleigh number of the second kind is larger for insulating side walls, and it is bounded by the limiting case of no side wall, which becomes unstable at a Rayleigh number of 4×10^5 (e.g. Mitrovica & Jarvis 1987). The influence of side walls on stability may be seen more systematically when the Rayleigh

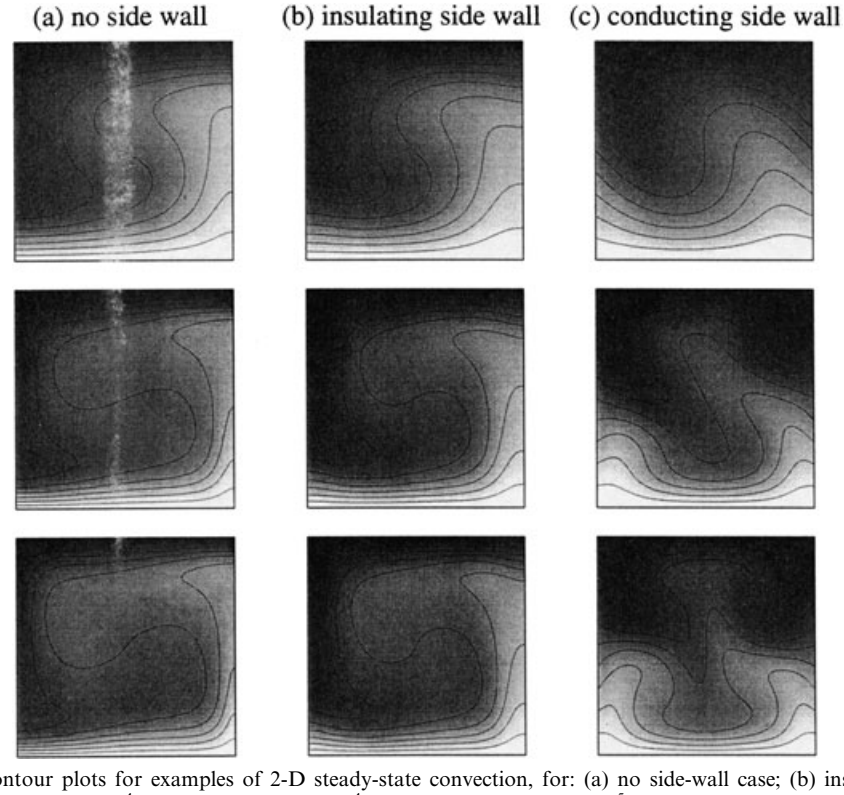

Figure 5. Temperature contour plots for examples of 2-D steady-state convection, for: (a) no side-wall case; (b) insulating side-wall case; and (c) conducting side-wall case, at $Ra = 10^4$ (top panel), $Ra = 4 \times 10^4$ (middle panel) and $Ra = 10^5$ (bottom). The contour interval is 0.1.

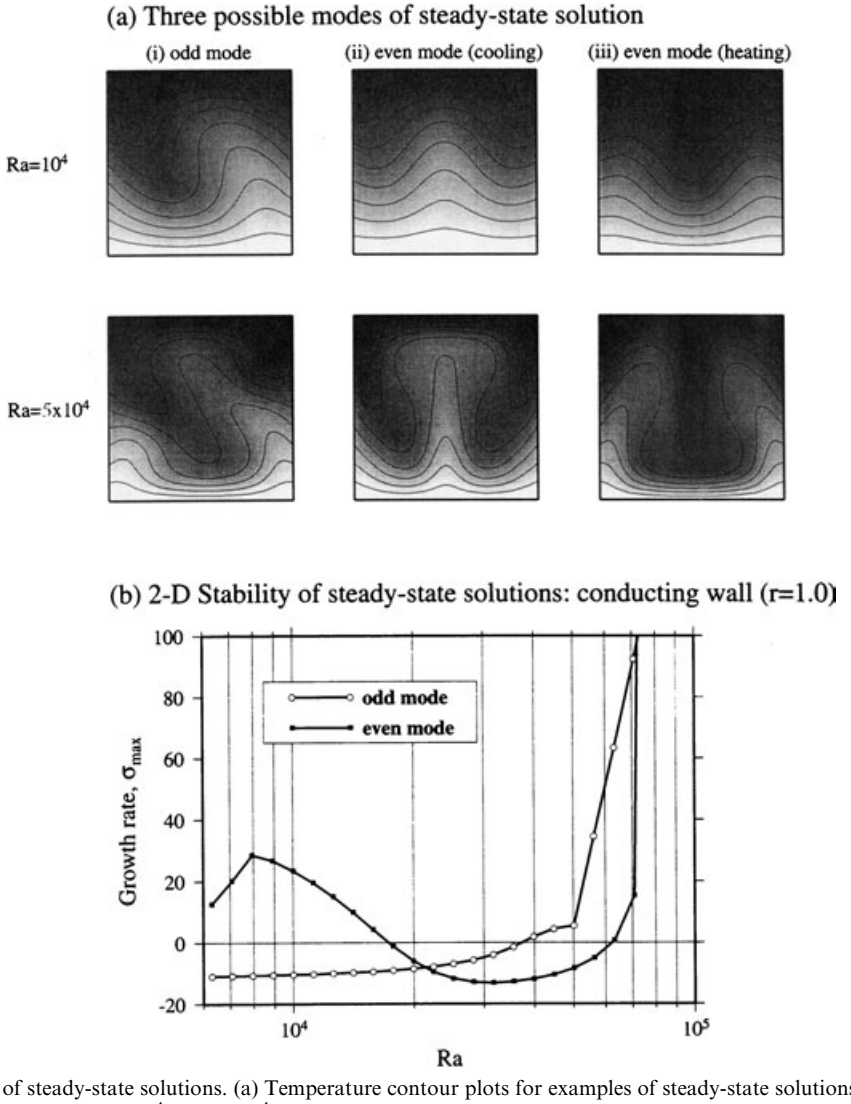

Figure 6. Non-uniqueness of steady-state solutions. (a) Temperature contour plots for examples of steady-state solutions for conducting side walls with an aspect ratio of 1, obtained at $Ra = 10^4$ and 5×10^4. (b) Growth exponents for the above steady-state solutions are plotted as a function of *Ra*. Open circles and solid squares denote the stability curve of the odd- and even-mode solutions, respectively.

number is normalized with the system's own critical value (Fig. 7). That conducting side walls are more destabilizing than insulating side walls can be understood in terms of thermal boundary layer instability. Following Howard (1966), we define the local Rayleigh number as

$$Ra_{\mathrm{l}} = \frac{\alpha \rho_{\mathrm{r}} g \Delta T_{\mathrm{l}} h^3}{\kappa \mu_{\mathrm{r}}}, \quad (19)$$

where ΔT_{l} is the temperature difference across a thermal boundary layer of thickness h. Because the conducting boundary condition leads to a thicker thermal boundary layer (e.g. Fig. 5), the local Rayleigh number is higher for conducting side walls than for insulating side walls at a given global Rayleigh number. Thus, the effects of a conducting side wall on thermal convection can be summarized by the two kinds of critical Rayleigh numbers, that is, a higher critical Rayleigh number and a lower transition Rayleigh number, compared with an insulating side wall. In other words, conducting side walls reduce the system's convective potential and, at the same time, increase the tendency for time-dependent convection.

5.3 Characteristics of 2-D convection in a bounded fluid

Two kinds of measures are used to characterize the strength of convection. The first one is the Nusselt number defined as

$$Nu = \frac{qd}{k\Delta T}, \quad (20)$$

where q is the heat flux averaged over a horizontal boundary and k is the thermal conductivity. *Nu* is the non-dimensional heat flux scaled by the conductive heat flux at a given temperature difference. A higher Nusselt number indicates more efficient heat transport realized by convection. The second measure of the strength of convection is the maximum vertical velocity. Our choice of a vertical velocity component rather than a horizontal velocity component is due to its relevance to terrestrial magmatism. When a vertical movement of mantle results in decompressional melting at shallow depths, vertical velocity becomes a critical parameter affecting the melt production rate. For high Rayleigh numbers where no stable

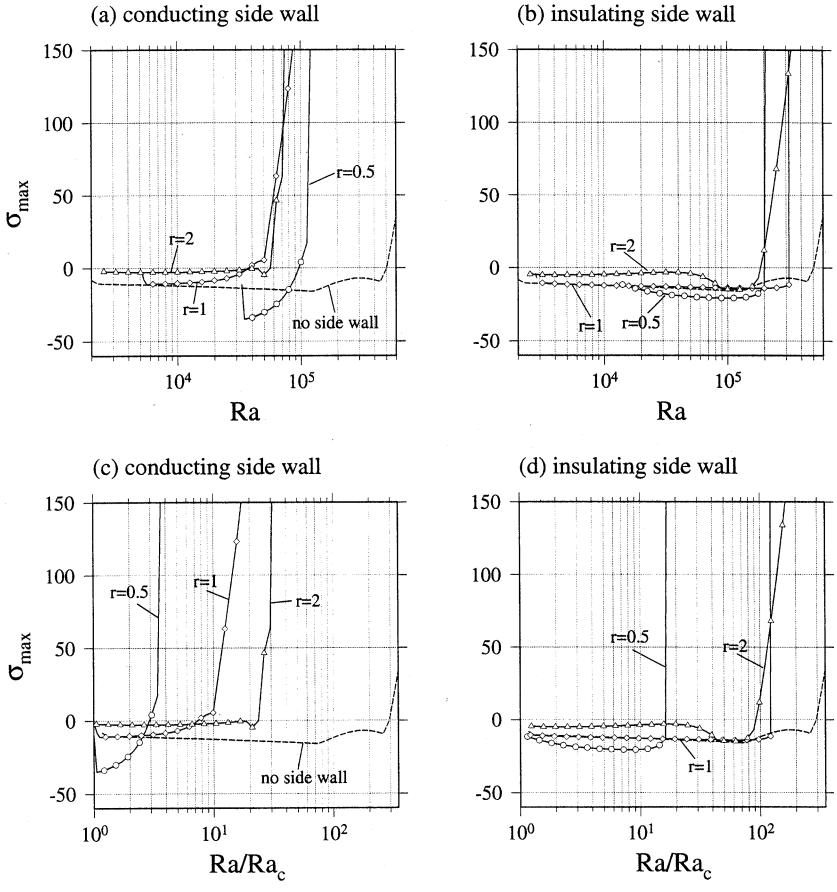

Figure 7. 2-D stability of 2-D steady-state convection. Growth exponents are shown for three aspect ratios (circle, $r=0.5$; diamond, $r=1$; and triangle, $r=2$) as a function of *Ra*, for (a) conducting side walls and (b) insulating side walls. The dashed curve denotes the stability curve for the limiting case with no side wall. Stability curves scaled with the system's own critical Rayleigh numbers are shown in (c) and (d).

steady-state solution exists, we conducted fully time-dependent calculations with an explicit time-stepping method. Starting from an artificial steady-state solution obtained by the temperature under-relaxation method, the system was integrated for a unit thermal diffusion time, which is equivalent to $\sim 10^3$–10^4 time steps for the range of Rayleigh numbers considered. Typically, the system reached its stationary state (i.e. a steady state in the time-averaged sense) within the first 0.1 diffusion time, and the time-averaged values of the Nusselt number and vertical velocity were then calculated for these stationary-state solutions. Results are presented in non-dimensionalized values, as well as dimensionalized ones scaled by relevant parameters appropriate for convection in the upper mantle: $d=600$ km, $\kappa=10^{-6}$ m^2 s^{-1}, $k=3.3$ W m^{-1} K^{-1} and $\Delta T=1300$ K.

For Rayleigh numbers in the range 10^4–10^6, the average Nusselt number and maximum vertical velocity are plotted in Fig. 8, for both conducting and insulating side walls. The case of no side wall is also shown as a reference. As expected from the extra constraints on convective motion imposed by side walls, both the Nusselt number and the vertical velocity are smaller in the bounded cases. The influence of the side walls is systematic—the system with a larger aspect ratio almost always shows higher values. Heat flux at a rigid boundary is essentially determined by the thickness of a thermal boundary layer, so that the very low Nusselt numbers for the conducting case with the Rayleigh number less than 10^5 result from the imposed, fixed-temperature condition on the vertical boundaries. For the Rayleigh number close to 10^6, the Nusselt numbers of the bounded cases are almost equal to that of the unbounded convection. This weakening of the side-wall effect on heat transfer at higher Rayleigh numbers has also been detected by theoretical and experimental studies on the relationship between *Nu* and *Ra* for convection bounded by insulating side walls (e.g. Frick & Clever 1982). Even for conducting side walls, the tendency to thicken thermal boundary layers and thus to lower the Nusselt number becomes negligible at higher Rayleigh numbers; a thick thermal boundary layer imposed by conductive side walls becomes unstable and is constantly destroyed, so the time-averaged Nusselt number increases.

In contrast, the vertical velocity is persistently affected by the presence of side walls. There is little difference between the different thermal boundary conditions. For an aspect ratio of 1.0, for example, about a factor of 2 reduction in the maximum vertical velocity can be observed for both kinds of side walls, up to the highest Rayleigh number we considered. One might expect that a scaling law for vertical velocity should behave similarly to that for heat flux, which is indeed the case for convection in an infinite horizontal layer (e.g. McKenzie *et al.* 1974). From this perspective, the observed discrepancy in the two scaling laws may be puzzling. This, however, can be understood by considering the kinetic energy budget. For a stationary state, the velocity is determined mainly by the balance between

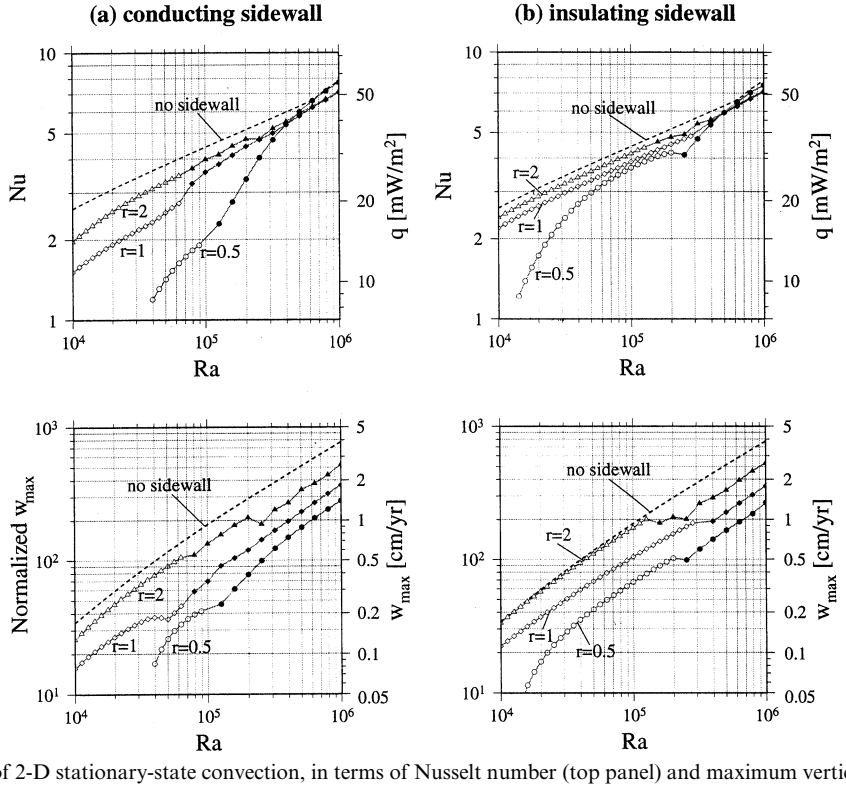

Figure 8. Characteristics of 2-D stationary-state convection, in terms of Nusselt number (top panel) and maximum vertical velocity (bottom panel), are plotted for: (a) conducting and (b) insulating cases. Open symbols denote measurements from steady-state solutions, and solid symbols those from time-dependent solutions. Three aspect ratios ($r=0.5$, 1 and 2) are considered. The dashed curve denotes the limiting case with no side wall. The statistics of time-dependent solutions are also used for the limiting case with $Ra>4\times10^5$, where no steady-state solution exists (Fig. 7).

the potential energy release and the energy dissipation at bounding surfaces (e.g. Chandrasekhar 1981). Whereas the growth of a horizontal thermal boundary layer is limited by the local Rayleigh number so that the Nusselt number becomes little affected by side walls, the kinematic effect of side walls is persistent. In other words, even though Nu is proportional to the square root of the convective velocity, as boundary layer theory predicts (e.g. Turcotte & Schubert 1982), the coefficient of this proportionality is different for side walls with a different aspect ratio. Nu must also be proportional to $\langle\theta w\rangle$, where θ denotes the temperature deviation from the horizontally averaged temperature and $\langle\rangle$ denotes horizontal averaging. Therefore, the persistent influence of side walls on w and not on Nu means that θ becomes more correlated with w as the Rayleigh number increases; this is consistent with the observation that high Nu is maintained by the convective destabilization of the thermal boundary layer.

One of the features of a stationary-state solution that is not evident in these scaling laws is the nature of temporal variability. Fig. 9 shows examples of stationary state solutions for the conducting side walls at two different Rayleigh numbers. For Rayleigh numbers slightly exceeding the transition value for time dependence, the temporal variation of observables such as the Nusselt number and the total kinetic energy is quasi-periodic with small amplitudes (Fig. 9a). As clearly seen from a series of snapshots of the temperature field, time dependence originates in boundary layer instabilities. Instabilities form near side walls, where the thermal boundary layer is thickest, and they grow inwards into the model domain. As the Rayleigh number increases, this periodic character diminishes, and more random, higher-frequency variation dominates with much larger amplitudes (Fig. 9b). It still appears that time dependence is controlled by instabilities at thermal boundary layers, but their occurrence is no longer limited to the vicinity of side walls.

A simple relation between the scale of time dependence and the Rayleigh number may be derived based on boundary layer theory, following the approach taken by Howard (1966). A thermal boundary layer becomes unstable when its local Rayleigh number reaches a threshold, Ra^δ,

$$Ra_l = Ra^\delta \tag{21}$$

The growth of a thermal boundary layer can be approximated as half-space cooling, so its thickness h may be expressed as $h\sim2\sqrt{\kappa t}$, where t is time. The corresponding temperature difference across the boundary layer is half of the total temperature difference across the entire model depth, $\Delta T/2$. Eqs (4), (19) and (21) can then be solved for the period, t_c, over which boundary layer instability repeats. The solution may be expressed as

$$\frac{t_c}{d^2/\kappa}=\left(\frac{Ra^\delta}{4Ra}\right)^{2/3}\sim\frac{25}{Ra^{2/3}}\,, \tag{22}$$

where we have assumed an Ra^δ of ~500 (Parsons & McKenzie 1978). Fig. 10 shows the power spectra of Nusselt numbers in the case of conducting side walls, for a range of Rayleigh numbers. Regardless of the aspect ratio of the bounded region, there is a broad agreement between the above, order-of-magnitude prediction and the actual measurements, in terms of the highest frequency excited. The effect of side walls is to

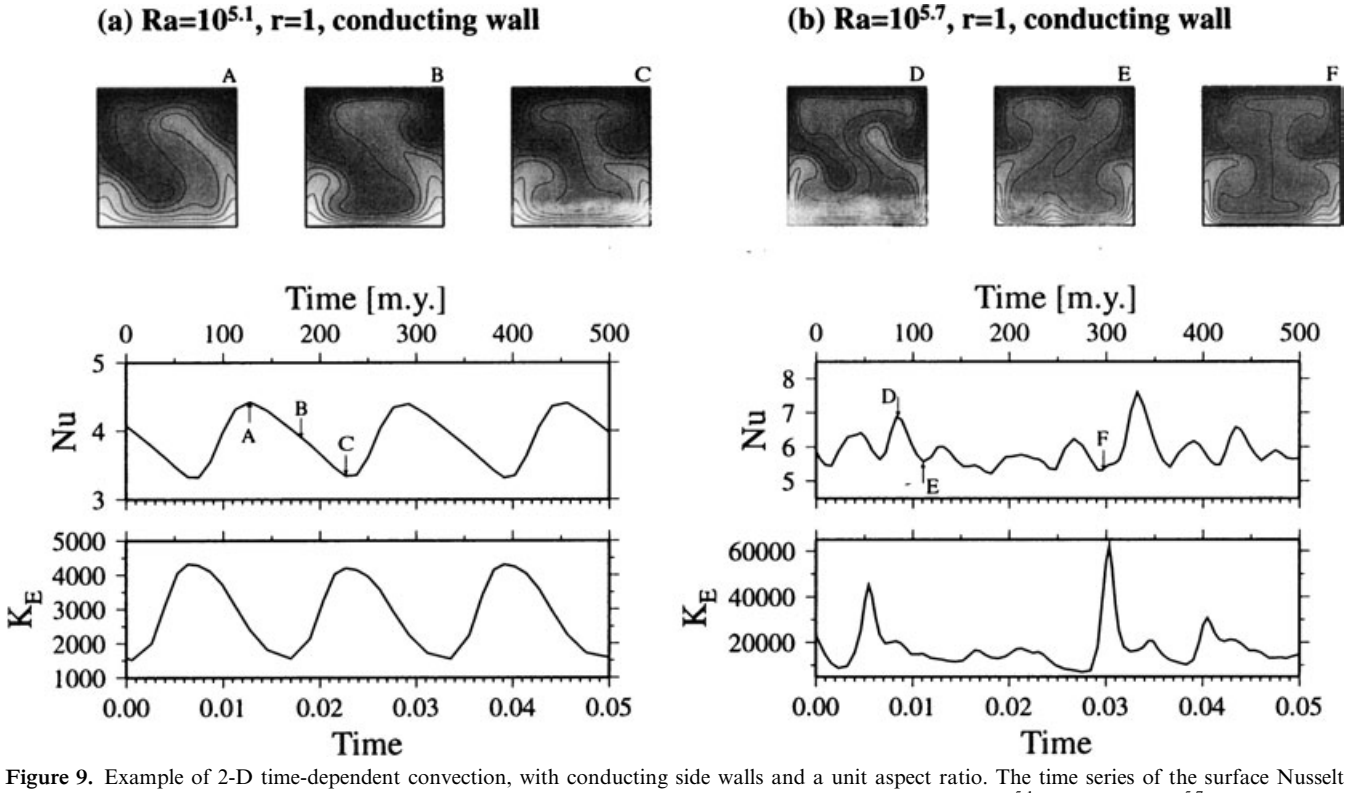

Figure 9. Example of 2-D time-dependent convection, with conducting side walls and a unit aspect ratio. The time series of the surface Nusselt number and the total kinetic energy are shown with snapshots of the contoured temperature field. (a) $Ra = 10^{5.1}$ and (b) $Ra = 10^{5.7}$.

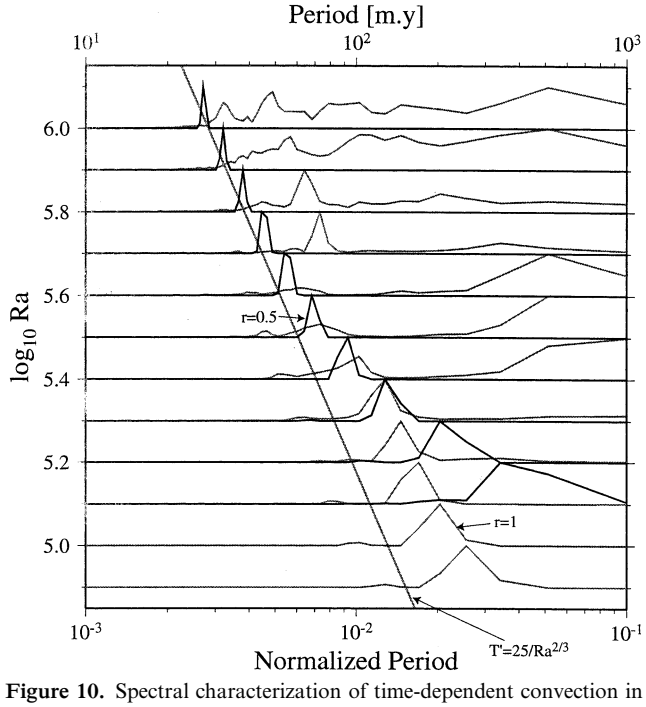

Figure 10. Spectral characterization of time-dependent convection in terms of the surface Nusselt number. The power spectrum of temporal variations in surface Nusselt numbers is plotted for a range of Rayleigh numbers. Solid lines denote the case of $r = 0.5$, and grey lines denote the case of $r = 1$. A theoretical estimate based on boundary layer theory is also shown.

lower the transition Rayleigh number for time-dependent behaviour, and the periodicity of boundary layer instability is simply related to the actual Rayleigh number itself, not to that scaled by the system's own critical Rayleigh number.

5.4 Stability for 3-D perturbations

The stability analysis of 2-D steady-state solutions can be extended to a full 3-D perturbation analysis, in a manner similar to the 3-D marginal stability analysis. For each 2-D steady-state solution, a growth exponent was first calculated as a function of the out-of-plane wavenumber, and its maximum value was then taken to determine the 3-D stability of the given 2-D solution. For the conducting case, the growth exponent is always positive from the marginally stable state, and it increases rapidly as the Rayleigh number increases (Fig. 11a). The stability curve for the insulating case shows a very different dependence on the Rayleigh number (Fig. 11b). The growth exponent is generally much smaller than that of the conducting case, and it becomes negative for a certain range of the Rayleigh number. The growth exponent is negative for *Ra* of $10^{3.85}$–$10^{4.5}$ with an aspect ratio of 1.0, and for *Ra* of $10^{3.45}$–$10^{4.4}$ with an aspect ratio of 2.0. The stability curve for an aspect ratio of 0.5 shows a gradual decrease as the Rayleigh number increases, but it never becomes zero for the range of Rayleigh number we have studied. This limited stability of a 2-D solution was also observed for convective systems with an infinite horizontal extent for *Ra* less than $10^{4.35}$ (Busse 1967; Clever & Busse 1974). In most cases, the most unstable wavenumber lies

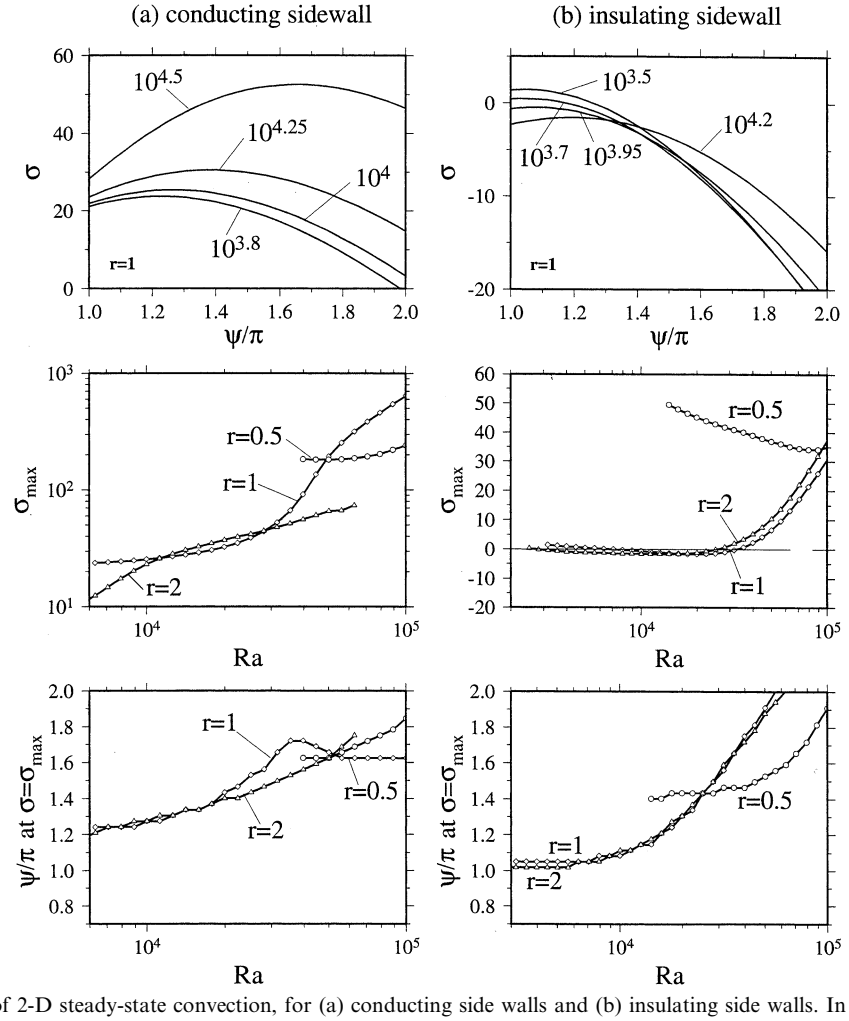

Figure 11. 3-D stability of 2-D steady-state convection, for (a) conducting side walls and (b) insulating side walls. In the top panels, the growth exponent σ in the case of a unit aspect ratio is plotted as a function of the out-of-plane wavenumber ψ, at several Rayleigh numbers (given on the graph). The maximum growth exponent and the corresponding out-of-plane wavenumber are shown in the middle and bottom panels, respectively, for three aspect ratios.

between π and 2π for the Rayleigh numbers we have investigated, and there is an overall increasing trend with increasing Rayleigh number.

Based on a comparison of stability curves for the two different thermal boundary conditions on side walls, we see that heat conduction through side walls has a large effect on the pattern of convection. In the marginal stability analysis, 3-D perturbations are always more destabilizing than 2-D perturbations, regardless of the thermal boundary condition, so that the negative growth exponents calculated for 3-D perturbations in systems with insulating side walls may be surprising. We note that, even for conducting side walls, single-mode 3-D perturbations are not always destabilizing if the out-of-plane wavenumber is sufficiently large ($>2\pi$); we see in Fig. 11(a) that the growth exponent is decreasing towards zero as the wavenumber increases. Negative growth exponents for some 2-D steady-state solutions for insulating side walls result from their stability even for low out-of-plane wavenumbers. Conducting side walls are more relevant to geophysical applications, however, and our stability analysis demonstrates that 3-D convective motion is fundamentally important for thermal convection bounded by conducting side walls. In the next section, therefore, we will investigate the nature of such a 3-D convection.

6 3-D CONVECTION IN A BOUNDED FLUID

Instead of solving a fully 3-D convection problem, we employ a single-mode approximation to the out-of-plane coordinate. Only one characteristic wavenumber is considered to represent convective cells aligned perpendicular to side walls. The 3-D single-mode approximation, conceptually similar to the mean-field approximation (Malkus 1954; Herring 1963), reduces the dimension of the system by one, so fewer computational resources are required compared with a fully 3-D case. Though the details of a single-mode solution, of course, depend on the prescribed out-of-plane wavenumber and are expected to be different from those of a fully 3-D solution, the 3-D single-mode approximation is an efficient way to evaluate the effect of the increased degree of freedom on domain-wide observables such as the Nusselt number. Care must be taken, however, not to overinterpret our results, because it is known that the Nusselt number based on a 2-D mean-field solution is systematically higher than that of a fully 2-D solution (Quareni *et al.* 1985; Quareni & Yuen 1988). Olson (1987) ascribed this systematic bias to the fact that the vertical velocity and temperature in the out-of-plane coordinate are perfectly correlated in 2-D

mean-field solutions. The effect of this perfect correlation should be somewhat reduced in our 3-D single-mode solutions, in which the basic-field temperature is 2-D and has its own velocity field. We will discuss several caveats for using the 3-D single-mode approximation in a subsequent section, by comparing with a fully 3-D solution.

In all calculations, we use the out-of-plane wavenumber of π, which corresponds to cellular convection with a unit aspect ratio. Only a conducting boundary condition is considered for side walls.

6.1 3-D single-mode approximation

We apply a single-mode approximation with a particular wavenumber, ψ, for the out-of-plane coordinate, y:

$$T(x, y, z) = T(x, z) + \theta(x, z)\cos(\psi y) \tag{23}$$

for a temperature field,

$$P(x, y, z) = P(x, z) + p(x, z)\cos(\psi y) \tag{24}$$

for a pressure field, and

$$\mathbf{u}(x, y, z) = \mathbf{U}(x, z) + \mathbf{u}_1(x, y, z) \tag{25}$$

for a velocity field, where

$$\mathbf{U}(x, z) = (U(x, z), 0, W(x, z)) \tag{26}$$

and

$$\mathbf{u}_1(x, y, z) = (u_1(x, z)\cos(\psi y), v_1(x, z)\sin(\psi y), w_1(x, z)\cos(\psi y)) . \tag{27}$$

We call $T(x, z)$ the basic-field temperature and $\theta(x, z)$ the deviation temperature. A similar nomenclature is used for the pressure and velocity. The system of thermal convection equations can then be written as:

(1) conservation of mass

$$\frac{\partial U}{\partial x} + \frac{\partial W}{\partial z} = 0 , \tag{28}$$

$$\frac{\partial u_1}{\partial x} + \psi v_1 + \frac{\partial w_1}{\partial z} = 0 ; \tag{29}$$

(2) conservation of momentum

$$-\nabla P + \nabla^2 \mathbf{U} - Ra\, T \mathbf{e}_z = 0 , \tag{30}$$

$$-\nabla p \cos(\psi y) + \nabla^2 \mathbf{u}_1 - Ra\, \theta \cos(\psi y)\mathbf{e}_z = 0 ; \tag{31}$$

(3) conservation of energy

$$\frac{\partial T}{\partial t} + U\frac{\partial T}{\partial x} + W\frac{\partial T}{\partial z} + \frac{1}{2}\left(u_1\frac{\partial \theta}{\partial x} - \psi v_1 \theta + w_1\frac{\partial \theta}{\partial z}\right) = \frac{\partial^2 T}{\partial x^2} + \frac{\partial^2 T}{\partial z^2} , \tag{32}$$

$$\frac{\partial \theta}{\partial t} + U\frac{\partial \theta}{\partial x} + W\frac{\partial \theta}{\partial z} + u_1\frac{\partial T}{\partial x} + w_1\frac{\partial T}{\partial z} = \frac{\partial^2 \theta}{\partial x^2} - \psi^2\theta + \frac{\partial^2 \theta}{\partial z^2} . \tag{33}$$

Because the basic-field velocity and the deviation velocity are completely decoupled in the equations of mass and momentum conservation, they are solved separately using a 2-D Stokes-flow solver and a 3-D single-mode Stokes-flow solver, respectively, for given temperature fields. A 2-D finite-element procedure has been developed to solve the equations of energy conservation, and its implementation is presented in Appendix B. Using these finite-element solvers, a steady-state solution can be obtained with the temperature relaxation method in the same manner as for 2-D convection. For all Rayleigh numbers from 10^4 to 10^6, steady-state solutions are easily obtained with a moderate relaxation factor. We do not attempt to investigate their stability, because they are likely to be artificially stabilized by the imposed symmetry in the out-of-plane coordinate.

6.2 Results

By inspecting the above equations, it can be shown that basic-field and deviation temperature fields must have the same type of reflecting symmetry with respect to a vertical plane. Because the most fundamental mode in deviation temperature is even [i.e. $\sin(\pi x)\sin(\pi z)$], even-mode solutions are generally preferred over odd-mode solutions, and indeed odd-mode solutions have much weaker velocity fields. Because of its $\cos(\psi y)$ dependence, the odd-mode out-of-plane temperature field corresponds to convection cells with an interchanging direction of convection. Such a planform of convection is expected to be unstable, and we were able to obtain odd-mode solutions only at low Rayleigh numbers ($\sim 10^4$) by the temperature under-relaxation method. There are two equivalent, stable, even-mode solutions, i.e. cooling and heating modes (e.g. Fig. 6), and only cooling-mode solutions are presented here, considering their relevance to the cooling effect of the cratonic lithosphere on upper-mantle convection, which is our primary interest. In general, the heat flux at the top and bottom boundaries can be different for even-mode solutions, and we take a logarithmic average of the top and bottom Nusselt numbers. Similarly, a logarithmic average of the absolute values of maximum upward and downward vertical velocities is calculated as a second measure of convective strength. This averaging eliminates the dependence of the following results on our choice of cooling- or heating-mode solutions.

Examples of temperature fields are shown in Fig. 12, and their 3-D rendition is shown in Fig. 13 with velocity fields. At an Ra of 10^4, reflection symmetry with respect to a horizontal plane is nearly maintained, so the difference between cooling and heating modes is small. Convective motion is almost entirely driven by the deviation temperature at this low Rayleigh number. As Ra increases, the degeneration of the two even-mode solutions disappears, and complex interactions between the basic-field and deviation temperature are observed. Higher Ra leads to a thinner thermal boundary layer, and because of the conducting boundary condition, a thermal boundary layer also develops along the side walls. This confinement of buoyancy to the vicinity of the model boundaries generates a centre upwelling in the basic-field velocity.

The average Nusselt number and average maximum vertical velocity of these steady-state solutions are summarized in Fig. 14. For comparison, values for the case of no side wall, obtained using 2-D mean-field and fully 2-D calculations are also shown. As already noted, 2-D mean-field solutions consistently overestimate the Nusselt number (Fig. 14a); a similar overestimation of Nu by 3-D single-mode calculations may explain why some of our values for a bounded fluid exceed the values of the unbounded case. Though an accurate estimate of the side-wall effect on the heat flux is thus difficult to obtain from 3-D single-mode solutions, we can infer that the side-wall effect on heat

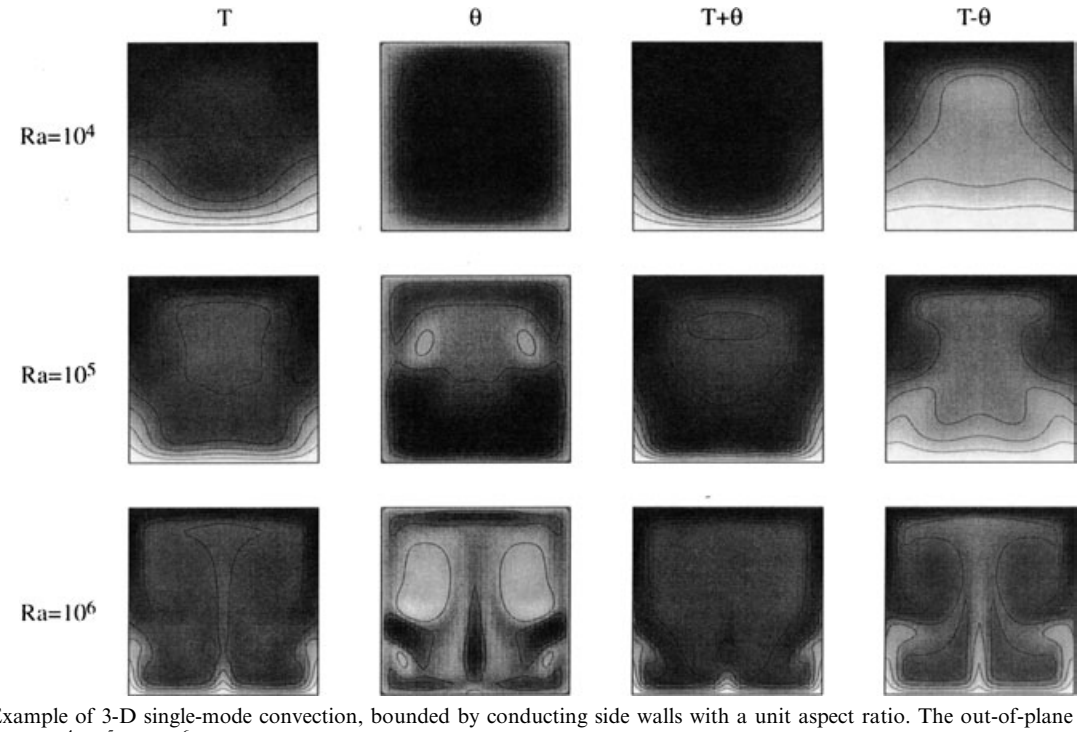

Figure 12. Example of 3-D single-mode convection, bounded by conducting side walls with a unit aspect ratio. The out-of-plane wavenumber is set as π. For $Ra = 10^4$, 10^5 and 10^6, basic-field and deviation temperature fields are shown along with slices at $y = 0$ and 1. Contour intervals are 0.1, except for the deviation temperature field, for which intervals are 0.05.

transfer is negligible for *Ra* greater than 10^5, based on a gross similarity among different aspect ratios. The Rayleigh number that marks this transition is about an order of magnitude lower than that for 2-D convection (Fig. 8a). Maximum vertical velocities in 3-D single-mode solutions (Fig. 14b) are approximately 50 per cent higher than those in 2-D solutions (Fig. 8b), regardless of the aspect ratio. The maximum velocity in the case of an aspect ratio of 2 slightly exceeds that of the limiting no side-wall case for *Ra* larger than 2×10^4, and this may again be due to the single-mode approximation. We may argue, however, that the influence of the single-mode approximation does not significantly degrade the velocity estimate. Because a fluid is not bounded in the out-of-plane coordinate, the observed 50 per cent increase in velocity compared with the purely 2-D case is what we may expect as a result of increasing the system's dimension from two to three, based on a balance between potential energy release and energy dissipation along rigid boundaries.

We define the 2-D basic-field kinetic energy as

$$\mathrm{KE_{bf}} = \int_V \left(\frac{\int \mathbf{u} dy}{\int dy} \right)^2 dV = \int_V (U^2 + W^2) dV \,. \tag{34}$$

The ratio of the 2-D basic-field kinetic energy to the total kinetic energy (Fig. 14c) shows the systematic influence of the aspect ratio. This ratio is a good measure of the two-dimensionality of a 3-D flow field. At an *Ra* of 10^6 and with a unit aspect ratio, for example, basic-field convection involves more than 50 per cent of the total kinetic energy, and the total temperature field shows that a sheet-like upwelling at the model centre dominates the convective system (Fig. 13). Because only one out-of-plane mode is treated in our 3-D single-mode calculation, this does not necessarily mean that a sheet-like upwelling is preferred to a cylindrical plume. A cylindrical plume involves a wide range of wavelengths, so it cannot be represented by our single-mode approximation.

6.3 Comparison with fully 3-D solutions

The 3-D single-mode approximation is only about twice as expensive both in computation time and memory usage, compared with a purely 2-D calculation. Because of this computational efficiency, it is a useful reconnaissance tool to evaluate the significance of 3-D convective motion. The use of the 3-D single-mode approximation is justified, however, only when the convective planform is expected to be dominantly linear. For example, applying the single-mode approximation when a hexagonal cell pattern is expected would be awkward. In addition, as we have already noted, one needs to be careful when interpreting 3-D single-mode solutions as they are merely a crude approximation of full three-dimensionality. Thus, it is desirable to compare 3-D single-mode solutions with equivalent fully 3-D solutions, to obtain some quantitative estimates on the reliability of the single-mode approximation. To this end, we conducted fully 3-D calculations for the case of conducting side walls with $r = 1.0$. We used a full multigrid 3-D convection code, the implementation of which is similar to that of Moresi & Gurnis (1996) (the mixed formulation with the pressure correction algorithm) and Zhong *et al.* (2000) (the full multigrid method with the consistent projection scheme). Assuming an even-mode solution, only half a domain ($0 \le x \le 0.5$, $0 \le y \le 1.0$ and $0 \le z \le 1.0$) is modelled with $16 \times 32 \times 32$ uniform trilinear elements. The system was integrated until it reached its steady state based on several measures of convection such as heat flux and maximum velocity. The range of *Ra* that we report here

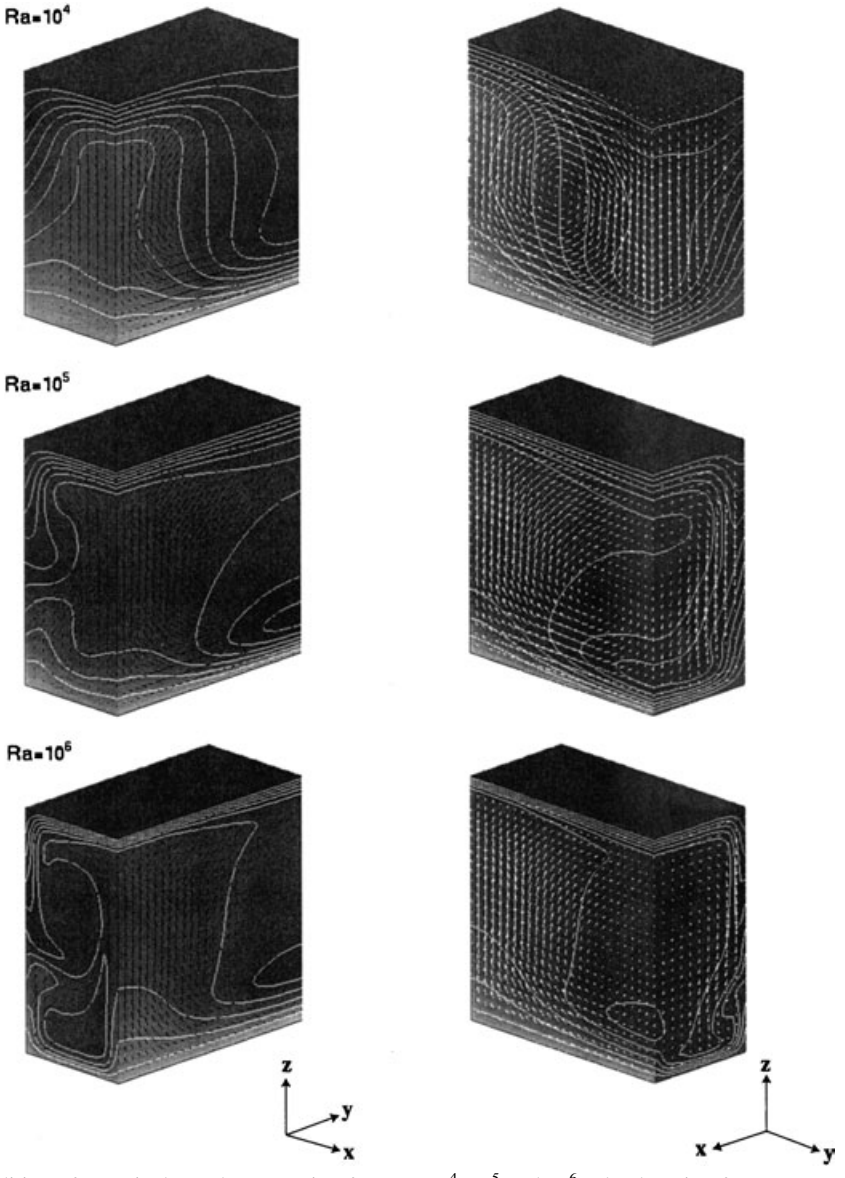

Figure 13. Perspective rendition of 3-D single-mode convection for $Ra = 10^4$, 10^5 and 10^6. The domain of $0 \le x \le 0.5$, $0 \le y \le 1.0$ and $0 \le z \le 1.0$ is shown, in its front view (left) and back view (right). Temperature contours are at a 0.1 interval. Velocity arrows are also shown, and their scale is normalized to the maximum value at each *Ra*.

is 10^4–10^5, for which the grid resolution is considered to be sufficiently fine. Grid refinement would be necessary to treat *Ra* higher than 10^5, for which the system also begins to exhibit a time dependence, requiring the integration of many time steps to obtain an accurate temporal average.

The results of fully 3-D calculations are shown in Fig. 15. As expected, it is found that the 3-D single-mode approximation consistently overpredicts the Nusselt number (Fig. 15a). The degree of overprediction is, however, much smaller than that of the 2-D mean-field approximation (Fig. 14a); the error in the Nusselt number is 6–9 per cent on an absolute scale and ~ 7 per cent on a logarithmic scale. This suggests that correlation between the vertical velocity and the temperature perturbation in the 3-D single-mode approximation is more realistic owing to the increased degree of freedom (i.e. two-dimensionality) for the basic field. In turn, the maximum vertical velocity is shown to be consistently underpredicted by the single-mode approximation (Fig. 15b). Though the prediction error on the absolute scale increases from ~ 3 per cent at $Ra = 10^4$ to ~ 9 per cent at $Ra = 10^5$, the error on the logarithmic scale is consistently smaller than 2 per cent. Despite these promising results on *Nu* and the maximum vertical velocity, the single-mode approximation behaves poorly in terms of flow patterns as *Ra* increases. The proportion of the basic-field component in the total kinetic energy (KE_{bf}/KE_{total}) increases almost linearly with *Ra* in fully 3-D solutions, whereas it starts to increase rapidly for $Ra > 10^{4.5}$ in the single-mode approximation (Fig. 15c). From the perspective of 3-D solutions, one can see that the fully 3-D flow field remains symmetric for upwelling and downwelling even at an *Ra* of 10^5 (Fig. 15e), and that this symmetry is maintained by exciting higher out-of-plane modes. This suggests that the kinetic energy corresponding to higher modes in fully

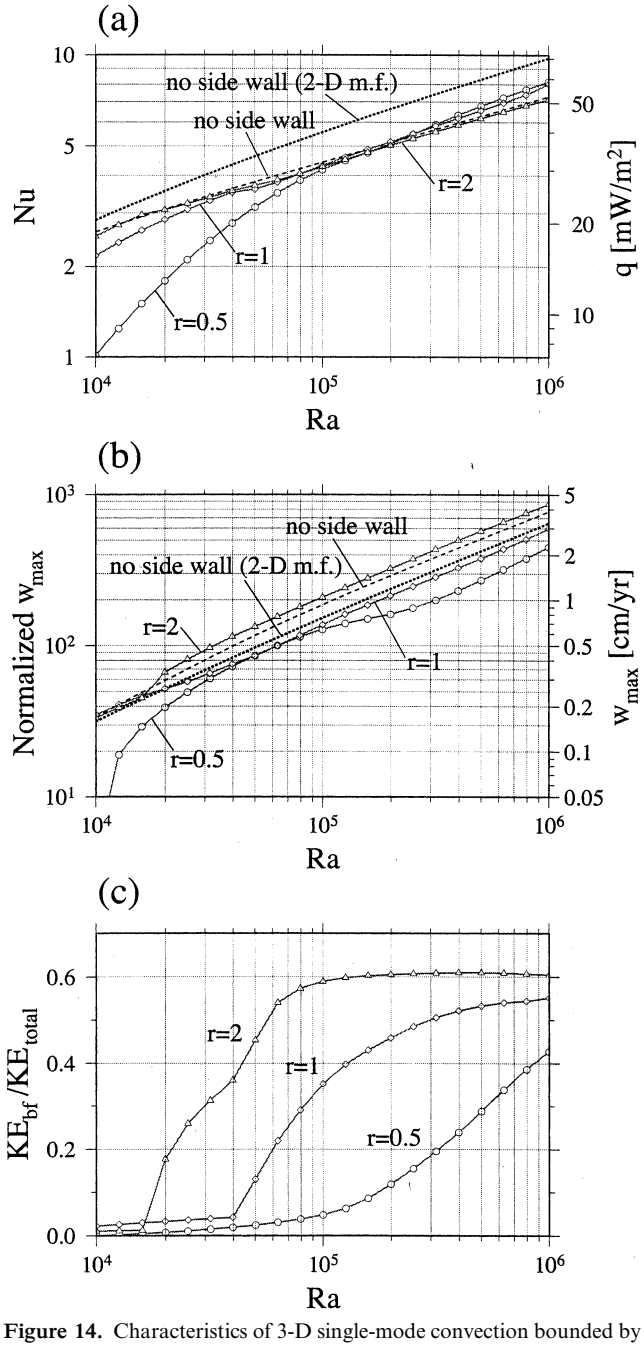

Figure 14. Characteristics of 3-D single-mode convection bounded by conducting side walls. The out-of-plane wavenumber is π. (a) Average Nusselt number and (b) average maximum velocity are plotted with open symbols for three aspect ratios (circle, $r=0.5$; diamond, $r=1$; and triangle, $r=2$). The dashed curve denotes the classical case with no side wall and the dotted curve denotes its 2-D mean-field approximation. (c) The proportion of basic-field kinetic energy (KE_{bf}/KE_{total}) is plotted as a function of the Rayleigh number.

3-D solutions is carried by the 2-D basic field in the 3-D single-mode approximation. Having only one out-of-plane mode, therefore, tends to exaggerate the two-dimensionality of the total 3-D flow field. It is interesting that, despite this important difference in flow patterns, the effects of 3-D convective motion on *Nu* and convective velocity are well captured by the single-mode approximation.

7 DISCUSSION

In our idealized model configuration, the influence of side walls is maximized. In the Earth, the continental lithosphere does not extend to the base of the upper mantle, and the variation in thickness is more diffuse, so that our study can be taken as a limiting case. We believe that this study is a necessary step towards a comprehensive understanding of small-scale mantle convection. A wide variety of lithospheric structure along continental margins is expected on the Earth, and site-specific modelling with realistic rheology is of course important. Our understanding of mantle rheology and of initial and boundary conditions is, however, often very limited. The purpose of a modelling study is to understand causes and consequences interweaved in a complex physical system. Conducting a large number of sets of convection simulations with different combinations of material properties, initial and boundary conditions, and so on, may only lead to the intractable proliferation of solutions without a comparable gain in understanding. A systematic study with more simplified models, therefore, must also be employed, which can provide a guideline in interpreting more complex models. These types of theoretical studies were beneficial to the development of the theory of (global-scale) mantle convection in the past, but such an approach has not been widely appreciated in the studies of small-scale convection.

For a conducting side wall, we used a linear thermal profile, because it is the simplest choice and retains reflection symmetry, which facilitates the calculation of steady-state solutions and stability analyses. It is obvious from the variational formulation that heat conduction at side walls always results in a higher critical Rayleigh number compared with insulation, regardless of the shape of the imposed temperature profile. In a strongly convecting regime, however, the influence of conducting side walls may be significantly modified by specifying different temperature profiles. Rabinowicz *et al.* (1980) and Nataf *et al.* (1981), for example, investigated the effect of a uniformly cold side wall, and found that lateral cooling led to the generation of convection cells with a wide aspect ratio. Their studies were designed to model cooling by a subducting slab, and efficient heat transfer at a side wall can result in additional negative buoyancy to overcome side-wall resistance. In this regard, our linear temperature profile minimizes the cooling effect of a geological side wall. Our primary interest, however, is in studying the effect of a thick, cratonic lithosphere on mantle convection, not the effect of slab cooling. Because of low continental heat flow and a high concentration of radiogenic elements in the continental crust, the estimated thermal structure of the cratonic lithosphere only suggests a moderate cooling effect of cratonic side walls adjacent to an asthenospheric mantle (Jordan 1988; Rudnick *et al.* 1998). The linear thermal profile used in this study, therefore, does not limit the application of our results to small-scale mantle convection associated with a cratonic lithosphere.

The effect of a cratonic lithosphere on mantle convection has been studied recently by King & Anderson (1995, 1998), with the focus on the relative importance of small-scale, edge-driven convection to large-scale background convection. Most of their calculations are limited to instantaneous Stokes flow generated by a few types of prescribed temperature fields. Their conclusions thus depend strongly on the nature of the background temperature field. For example, a strong upwelling from the base of the cratonic lithosphere towards the thin lithosphere, as

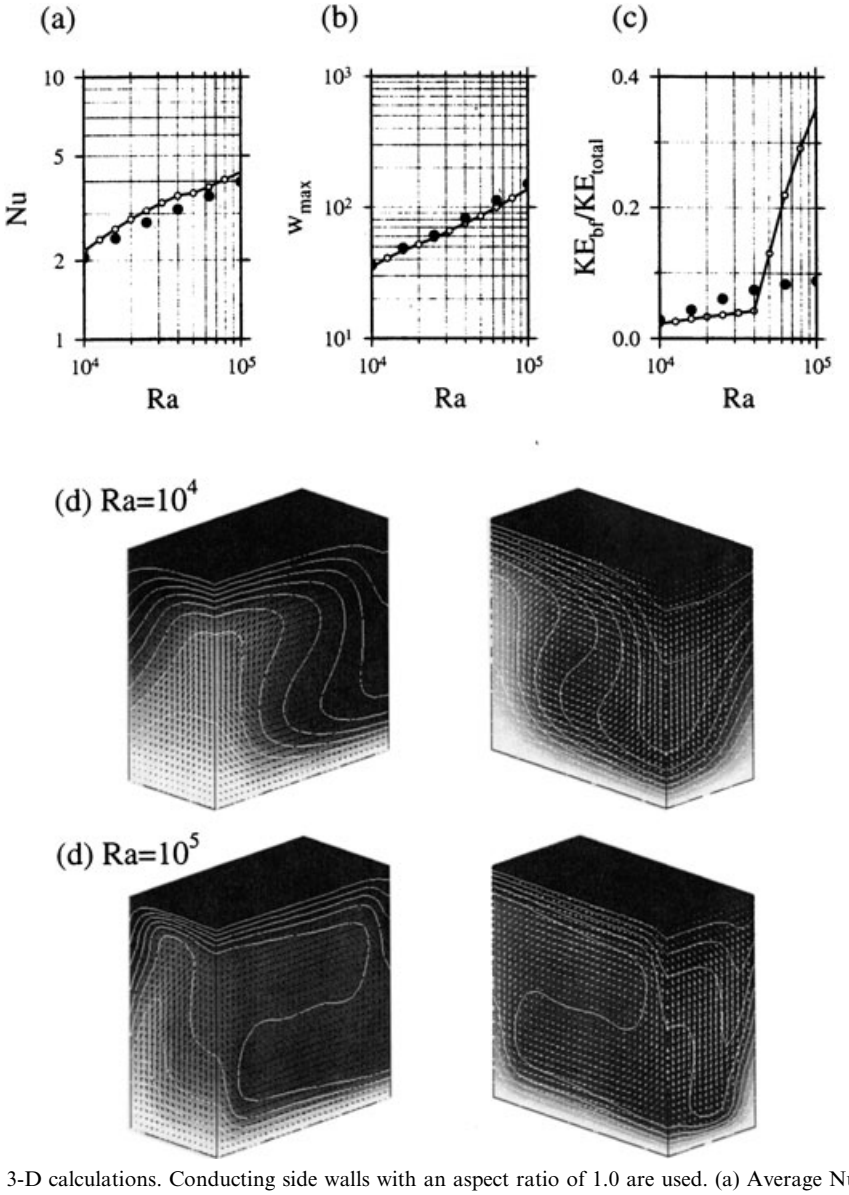

Figure 15. Results of fully 3-D calculations. Conducting side walls with an aspect ratio of 1.0 are used. (a) Average Nusselt number; (b) average maximum velocity; and (c) KE_{bf}/KE_{total} are plotted as a function of *Ra* (solid circles). A 3-D single-mode approximation is also plotted for comparison (open circles). A perspective rendition is also shown as in Fig. 13 for (d) $Ra = 10^4$ and (e) $Ra = 10^5$.

observed in their model, is a variant of classical Rayleigh–Bénard convection deformed by the top rigid boundary. Their temperature field is designed to place a wide convection cell beneath a continent–ocean boundary, and the coincidence of upwelling and a continent–ocean boundary should not be taken as being the effect of a cratonic lithosphere. Several time-dependent calculations in King & Anderson (1998) show that calculated Stokes flow does not sustain the initial temperature field. The influence of large-scale background flow is unarguably important for the study of small-scale convection, and a more self-consistent approach to generating pre-existing large-scale flow is necessary to draw some general conclusions.

The present study focuses on the stationary state of convection. It is thus useful to constrain the expected status of the mantle, in the absence of a temporal change in boundary conditions such as deformation of the lithosphere. Transient mantle dynamics caused by changes in boundary conditions, such as rifting-related convection (Mutter *et al.* 1988; Keen & Boutilier 1995; Boutilier & Keen 1999), has usually been studied with apparently innocuous initial conditions; the asthenospheric mantle is assumed to be initially isothermal and static. An asthenospheric mantle subject to surface cooling (and some mode of heating from below), however, must be convecting, and our study suggests that the distribution of a thick continental lithosphere can organize the pattern of such a convection, preferring convective rolls aligned perpendicular to continent–ocean boundaries. This may be relevant to some previous speculations concerning the effect of cratonic keels on mantle convection, based on the spatial association between cratons and continental flood basalt provinces (Anderson 1994) and between continental margins and hotspots (Vogt 1991; Anderson 1998b). Frequent occurrences of voluminous magmatism during continental break-ups may have originated in the combination of such modulated upper-mantle convection and slow surface rifting (e.g. Korenaga *et al.* 2000).

8 CONCLUSIONS

To understand the effect of lithospheric thickness variation on mantle convection, we have investigated a simple convection system in which a fluid is bounded by rigid side walls. Both conducting and insulating boundary conditions on side walls are considered to isolate kinematic and thermal effects. First, 2-D and 3-D marginal stability analyses show that heat conduction at side walls always reduces convective instability and generally favours convective rolls aligned perpendicular to side walls. The strength of thermal convection is characterized by the surface heat flux and the maximum vertical velocity for supercritical Rayleigh numbers. The presence of side walls becomes negligible for the heat flux at higher Rayleigh number, owing to the instability of thermal boundary layers, but its influence on the velocity is shown to be persistent. The nature of convective stability is then assessed by 2-D and 3-D stability analyses of 2-D steady-state solutions. Within a purely 2-D framework, side walls enhance the tendency towards time-dependent convection. The periodicity in a stationary state is related to the development of boundary layer instability, and it scales simply with the Rayleigh number. The 3-D stability analysis reveals the contrasting effects of the side-wall thermal boundary conditions on the planform of convection; conducting side walls strongly prefer 3-D convective motion. Finally, the characteristics of 3-D convection bounded by conducting side walls are thus studied through the 3-D single-mode approximation, and results indicate that side-wall effects are reduced in 3-D convection, for both heat transfer and vertical velocity, compared with the 2-D results. Comparison with fully 3-D solutions suggests that the 3-D single-mode approximation is an efficient tool for investigating the domain-wide characteristics of the 3-D convective motion such as the Nusselt number and maximum vertical velocity, though the approximation tends to underestimate the three-dimensionality of the flow structure. This study suggests that a thick, cratonic lithosphere may have a modulating effect on the planform of small-scale convection in the upper mantle, without significantly reducing the intrinsic convective strength.

ACKNOWLEDGMENTS

This work was sponsored by the U.S. National Science Foundation under grant EAR-0049044. We thank Jack Whitehead, Brad Hager and Don Anderson for constructive comments on an earlier version of this manuscript. Reviews by Shijie Zhong and an anonymous reviewer were very helpful in improving the clarity of the manuscript.

REFERENCES

Anderson, D.L., 1994. Superplumes or supercontinents?, *Geology,* **22,** 39–42.

Anderson, D.L., 1998a. The EDGES of the mantle, in *The Core–Mantle Boundary Region,* pp. 255–271, eds Gurnis, M., Wysession, M.E., Knittle, E. & Buffett, B.A. American Geophysical Union, Washington, DC.

Anderson, D.L., 1998b. The scales of mantle convection, *Tectonophysics,* **284,** 1–17.

Batchelor, G.K., 1954. Heat transfer by free convection across a closed cavity between vertical boundaries at different temperatures, *Q. appl. Math.,* **12,** 209–233.

Boutilier, R.R. & Keen, C.E., 1999. Small-scale convection and divergent plate boundaries, *J. geophys. Res.,* **104,** 7389–7403.

Brooks, A.N. & Hughes, T.J.R., 1982. Streamline upwind/Petrov–Galerkin formulations for convection dominated flows with particular emphasis on the incompressible Navier–Stokes equations, *Comp. Meth. Appl. Mech. Eng.,* **32,** 199–259.

Bunge, H., Richards, M.A., Lithgow-Bertelloni, C., Baumgardner, J.R., Grand, S.P. & Romanowicz, B.A., 1998. Time scales and heterogeneous structure in geodynamic earth models, *Science,* **280,** 91–95.

Busse, F.H., 1967. On the stability of two-dimensional convection in a layer heated from below, *J. Math. Phys.,* **46,** 140–150.

Busse, F.H., 1978. A model of time-periodic flow, *Geophys. J. R. astr. Soc.,* **52,** 1–12.

Chandrasekhar, S., 1981. *Hydrodynamic and Hydromagnetic Stability,* Dover, New York.

Charlson, G.S. & Sani, R.L., 1970. Thermoconvective instability in a bounded cylindrical fluid layer, *Int. J. Heat Mass Trans.,* **13,** 1479–1496.

Charlson, G.S. & Sani, R.L., 1971. On thermoconvective instability in a bounded cylindrical fluid layer, *Int. J. Heat Mass Trans.,* **14,** 2157–2160.

Chen, Y.-Y., 1992. Boundary conditions and linear analysis of finite-cell Rayleigh–Bénard convection, *J. Fluid Mech.,* **241,** 549–585.

Christensen, U., 1983. A numerical model of coupled subcontinental and oceanic convection, *Tectonophysics,* **95,** 1–23.

Christensen, U., 1984. Convection with pressure- and temperature-dependent non-Newtonian rheology, *Geophys. J.R. astr. Soc.,* **77,** 343–384.

Christensen, U.R., 1987. Time-dependent convection in elongated Rayleigh–Bénard cells, *Geophys. Res. Lett.,* **14,** 220–223.

Clever, R.M. & Busse, F.H., 1974. Transition to time-dependent convection, *J. Fluid Mech.,* **65,** 625–645.

Davaille, A. & Jaupart, C., 1993. Transient high-Rayleigh-number thermal convection with large viscosity variations, *J. Fluid Mech.,* **253,** 141–166.

Davis, S.H., 1967. Convection in a box: linear theory, *J. Fluid Mech.,* **30,** 465–478.

Elder, J., 1976. *The Bowels of the Earth,* Oxford University Press, Oxford.

Forte, A.M. & Mitrovica, J.X., 1996. New inferences of mantle viscosity from joint inversion of long-wavelength mantle convection and post-glacial rebound data, *Geophys. Res. Lett.,* **23,** 1147–1150.

Frick, H. & Clever, R.M., 1982. The influence of side walls on finite-amplitude convection in a layer heated from below, *J. Fluid Mech.,* **114,** 467–480.

Gaherty, J.B. & Jordan, T.H., 1995. Lehmann discontinuity as the base of an anisotropic layer beneath continents, *Science,* **268,** 1468–1471.

Grand, S.P., 1994. Mantle shear structure beneath the Americas and surrounding oceans, *J. geophys. Res.,* **99,** 11 591–11 621.

Hager, B.H. & O'Connell, R.J., 1981. A simple global model of plate dynamics and mantle convection, *J. geophys. Res.,* **86,** 4843–4867.

Hager, B.H., Clayton, R.W., Richards, M.A., Comer, R.P. & Dziewonski, A.M., 1985. Lower mantle heterogeneity, dynamic topography and the geoid, *Nature,* **313,** 541–545.

Hansen, U. & Ebel, A., 1988. Time-dependent thermal convection—a possible explanation for a multiscale flow in the Earth's mantle, *Geophys. J.,* **94,** 181–191.

Herring, J.R., 1963. Investigation of problems in thermal convection, *J. atmos. Sci.,* **20,** 325–338.

Hill, R.I., Campbell, I.H., Davies, G.F. & Griffiths, R.W., 1992. Mantle plumes and continental tectonics, *Science,* **256,** 186–193.

Honda, S., Yuen, D.A., Balachandar, S. & Reuteler, D., 1993. Three-dimensional instabilities of mantle convection with multiple phase transitions, *Science,* **259,** 1308–1311.

Howard, L.N., 1966. Convection at high Rayleigh number, in *Proc. 11th Int. Congress of Applied Mechanics,* pp. 1109–1115, ed. Gortler, H., Springer-Verlag, New York.

Hughes, T.J.R., 1987. *The Finite Element Method: Linear Static and Dynamic Finite Element Analysis,* Prentice-Hall, NJ.
Jordan, T.H., 1988. Structure and formation of the continental tectosphere, *J. Petrol. Spec. Vol.,* pp. 11–37.
Karato, S. & Wu, P., 1993. Rheology of the upper mantle: a synthesis, *Science,* **260,** 771–778.
Keen, C.E. & Boutilier, R.R., 1995. Lithosphere–asthenosphere interactions below rifts, in *Rifted Ocean–Continent Boundaries*, eds Banda, E., Torne, M. & Talwani, M., pp. 17–30, Kluwer, Dordrecht.
King, S.D. & Anderson, D.L., 1995. An alternative mechanism of flood basalt formation, *Earth planet. Sci. Lett.,* **136,** 269–279.
King, S.D. & Anderson, D.L., 1998. Edge-driven convection, *Earth planet. Sci. Lett.,* **160,** 289–296.
Korenaga, J., Holbrook, W.S., Kent, G.M., Kelemen, P.B., Detrick, R.S., Larsen, H., Hopper, J.R. & Dahl-Jensen, T., 2000. Crustal structure of the southeast Greenland margin from joint refraction and reflection seismic tomography, *J. geophys. Res.,* **105,** 21 591–21 614.
Le Quere, P. & Behnia, M., 1998. From onset of unsteadiness to chaos in a differentially heated square cavity, *J. Fluid Mech.,* **359,** 81–107.
Malkus, W.V.R., 1954. The heat transport and spectrum of thermal turbulence, *Proc. R. Soc. Lond.,* A**225,** 196–212.
McKenzie, D.P., Roberts, J.M. & Weiss, N.O., 1974. Convection in the Earth's mantle: towards a numerical simulation, *J. Fluid Mech.,* **62,** 465–538.
Mitrovica, J.X. & Jarvis, G.T., 1987. A numerical study of thermal convection between rigid horizontal boundaries, *Geophys. Astrophys. Fluid Dyn.,* **38,** 193–224.
Montagner, J.P. & Tanimoto, T., 1991. Global upper mantle tomography of seismic velocities and anisotropies, *J. geophys. Res.,* **96,** 20 337–20 351.
Moresi, L. & Gurnis, M., 1996. Constraints on the lateral strength of slabs from three dimensional dynamic flow models, *Earth planet. Sci. Lett.,* **138,** 15–28.
Moresi, L., Zhong, S. & Gurnis, M., 1996. The accuracy of finite element solutions of Stokes' flow with strongly varying viscosity, *Phys. Earth planet. Inter.,* **97,** 83–94.
Mutter, J.C., Buck, W.R. & Zehnder, C.M., 1988. Convective partial melting, 1, a model for the formation of thick basaltic sequences during the initiation of spreading, *J. geophys. Res.,* **93,** 1031–1048.
Nataf, H.C., Froidevaux, C., Levrat, J.L. & Rabinowicz, M., 1981. Laboratory convection experiments: effect of lateral cooling and generation of instabilities in the horizontal boundary layers, *J. geophys. Res.,* **86,** 6143–6154.
Olson, P., 1987. A comparison of heat transfer laws for mantle convection at very high Rayleigh numbers, *Phys. Earth planet. Inter.,* **48,** 153–160.
Parsons, B. & McKenzie, D., 1978. Mantle convection and the thermal structure of the plates, *J. geophys. Res.,* **83,** 4485–4496.
Quareni, F. & Yuen, D.A., 1988. Mean-field methods in mantle convection, in *Mathematical Geophysics,* pp. 227–264, eds Vlaar, N.J., Nolet, G., Wortel, M.J.R. & Cloetingh, S.A.P.L., Reidel, Dordrecht.
Quareni, F., Yuen, D.A., Sewell, G. & Christensen, U.R., 1985. High Rayleigh number convection with strongly variable viscosity: a comparison between mean field and two-dimensional solutions, *J. geophys. Res.,* **90,** 12 633–12 644.
Rabinowicz, M., Lago, B. & Froidevaux, C., 1980. Thermal transfer between the continental asthenosphere and the oceanic subducting lithosphere: its effect on subcontinental convection, *J. geophys. Res.,* **85,** 1839–1853.
Ravi, M.R., Henkes, R.A.W.M. & Hoogendoorn, C.J., 1994. On the high-Rayleigh-number structure of steady laminar natural-convection flow in a square enclosure, *J. Fluid Mech.,* **262,** 325–351.
Richards, M.A., Duncan, R.A. & Courtillot, V.E., 1989. Flood basalts and hot-spot tracks: plume heads and tails, *Science,* **246,** 103–107.
Richter, F.M., 1973a. Dynamical models for sea floor spreading, *Rev. Geophys. Space Phys.,* **11,** 223–287.
Richter, F.M., 1973b. Convection and the large-scale circulation of the mantle, *J. geophys. Res.,* **78,** 8735–8745.
Richter, F.M. & McKenzie, D.P., 1981. On some consequences and possible causes of layered mantle convection, *J. geophys. Res.,* **86,** 6133–6142.
Ritzwoller, M.H. & Lavely, E.M., 1995. Three-dimensional seismic models of the Earth's mantle, *Rev. Geophys.,* **33,** 1–66.
Rudnick, R.L., McDonough, W.F. & O'Connell, R.J., 1998. Thermal structure, thickness and composition of continental lithosphere, *Chem. Geol.,* **145,** 395–411.
Simons, F.J., Zielhuis, A. & van der Hilst, R.D., 1999. The deep structure of the Australian continent from surface wave tomography, *Lithos,* **48,** 17–43.
Simons, M. & Hager, B.H., 1997. Localization of the gravity field and the signature of glacial rebound, *Nature,* **390,** 500–504.
Solheim, L.P. & Peltier, W.R., 1994. Avalanche effects in phase transition modulated thermal convection, *J. geophys. Res.,* **99,** 6997–7018.
Solomatov, V.S., 1995. Scaling of temperature- and stress-dependent viscosity convection, *Phys. Fluids,* **7,** 266–274.
Solomatov, V.S. & Moresi, L., 2000. Scaling of time-dependent stagnant lid convection: application to small-scale convection on Earth and other terrestrial planets, *J. geophys. Res.,* **105,** 21 795–21 817.
Su, W., Woodward, R.L. & Dziewonski, A.M., 1994. Degree 12 model of shear velocity heterogeneity in the mantle, *J. geophys. Res.,* **99,** 6945–6980.
Tackley, P.J., 1995. On the penetration of an endothermic phase transition by upwellings and downwellings, *J. geophys. Res.,* **100,** 15 477–15 488.
Tackley, P.J., Stevenson, D.J., Glatzmaier, G.A. & Schubert, G., 1993. Effects of an endothermic phase transition at 670 km depth in a spherical model of convection in the Earth's mantle, *Nature,* **361,** 699–704.
Turcotte, D.L. & Schubert, G., 1982. *Geodynamics: Applications of Continuum Physics to Geological Problems,* Wiley, New York.
van der Hilst, R.D., Widiyantoro, S. & Engdahl, E.R., 1997. Evidence for deep mantle circulation from global tomography, *Nature,* **386,** 578–584.
Velte, W., 1964. Stabilitätsverhalten und Verzweigung stationärer Lösungen der Navier–Stokesschen Gleichungen, *Arch. Rat. Mech. Anal.,* **16,** 97–125.
Vogt, P.R., 1991. Bermuda and Appalachian–Labrador rises: common non-hotspot processes?, *Geology,* **19,** 41–44.
White, R. & McKenzie, D., 1989. Magmatism at rift zones: the generation of volcanic continental margins and flood basalts, *J. geophys. Res.,* **94,** 7685–7729.
Whitehead, J.A., 1988. Fluid models of geological hotspots, *Ann. Rev. Fluid Mech.,* **20,** 61–87.
Zhang, K. & Busse, F.-H., 1997. Convection in spherical fluid shells with an outer crust of variable thickness, *Phys. Earth planet. Inter.,* **104,** 283–294.
Zhang, Y.-S. & Tanimoto, T., 1993. High-resolution global upper mantle structure and plate tectonics, *J. geophys. Res.,* **98,** 9793–9823.
Zhong, S., Zuber, M.T., Moresi, L. & Gurnis, M., 2000. Role of temperature-dependent viscosity and surface plates in spherical shell models of mantle convection, *J. geophys. Res.,* **105,** 11 063–11 082.

APPENDIX A: FINITE-ELEMENT FORMULATION FOR 3-D SINGLE-MODE STOKES FLOW

Following the notation adopted by Hughes (1987), the Galerkin formulation of the equations of Stokes flow, eqs (1) and (2),

may be expressed as

$$\mathbf{Kd} = \mathbf{F}, \tag{A1}$$

where $\mathbf{K}$, $\mathbf{d}$ and $\mathbf{F}$ are a stiffness matrix, a velocity vector and a force vector, respectively. The stiffness matrix and the force vector are constructed by summing all elemental contributions:

$$\mathbf{K} = \mathop{A}_{e=1}^{n_{\mathrm{el}}} (\mathbf{k}^e), \quad \mathbf{F} = \mathop{A}_{e=1}^{n_{\mathrm{el}}} (\mathbf{f}^e), \tag{A2}$$

where A denotes the finite-element assembly operator, and $\mathbf{k}^e$ and $\mathbf{f}^e$ are the stiffness matrix and force vector of the eth element. Since the degree of freedom is three, $\mathbf{k}^e$ has dimensions $3n_{\mathrm{en}} \times 3n_{\mathrm{en}}$, where n_{en} is the number of element nodes. Using the following subscripts,

$$p = 3(a-1)+i, \quad q = 3(b-1)+j,$$

$$1 \le a, b \le n_{\mathrm{en}}, \qquad 1 \le i, j \le 3,$$

element stiffness matrices may be further decomposed as

$$k^e_{pq} = \mathbf{e}_i^{\mathrm{T}} k^e_{ab} \mathbf{e}_j, \quad k^e_{ab} = \bar{k}_{ab} + \bar{\bar{k}}_{ab}, \tag{A3}$$

where the penalty formulation is assumed in the second expression. Now introducing a 3-D flow field with a single wavenumber of ψ in the out-of-plane coordinate (note that we set the out-of-plane coordinate as the third coordinate in this formulation),

$$\mathbf{u}_1(x, y, z) = (u_1(x, z)\cos(\psi y), w_1(x, z)\cos(\psi y), v_1(x, z)\sin(\psi y)), \tag{A4}$$

the explicit form of element stiffness matrices can be obtained as follows:

$$\bar{k}_{ab,11} = \int_{\Omega^e} \mu(2N_{a,1}N_{b,1} + N_{a,2}N_{b,2} + \psi^2 N_a N_b) d\Omega, \tag{A5}$$

$$\bar{k}_{ab,12} = \int_{\Omega^e} \mu N_{a,2}N_{b,1} d\Omega, \tag{A6}$$

$$\bar{k}_{ab,13} = -\int_{\Omega^e} \mu\psi N_a N_{b,1} d\Omega, \tag{A7}$$

$$\bar{k}_{ab,21} = \int_{\Omega^e} \mu N_{a,1}N_{b,2} d\Omega, \tag{A8}$$

$$\bar{k}_{ab,22} = \int_{\Omega^e} \mu(N_{a,1}N_{b,1} + 2N_{a,2}N_{b,2} + \psi^2 N_a N_b) d\Omega, \tag{A9}$$

$$\bar{k}_{ab,23} = -\int_{\Omega^e} \mu\psi N_a N_{b,2} d\Omega, \tag{A10}$$

$$\bar{k}_{ab,31} = -\int_{\Omega^e} \mu\psi N_{a,1} N_b d\Omega, \tag{A11}$$

$$\bar{k}_{ab,32} = -\int_{\Omega^e} \mu\psi N_{a,2} N_b d\Omega, \tag{A12}$$

$$\bar{k}_{ab,33} = \int_{\Omega^e} \mu(N_{a,1}N_{b,1} + N_{a,2}N_{b,2} + 2\psi^2 N_a N_b) d\Omega, \tag{A13}$$

and

$$\bar{\bar{k}}_{ab,11} = \int_{\Omega^e} \lambda N_{a,1}N_{b,1} d\Omega, \tag{A14}$$

$$\bar{\bar{k}}_{ab,12} = \int_{\Omega^e} \lambda N_{a,1}N_{b,2} d\Omega, \tag{A15}$$

$$\bar{\bar{k}}_{ab,13} = \int_{\Omega^e} \lambda\psi N_{a,1} N_b d\Omega, \tag{A16}$$

$$\bar{\bar{k}}_{ab,21} = \int_{\Omega^e} \lambda N_{a,2}N_{b,1} d\Omega, \tag{A17}$$

$$\bar{\bar{k}}_{ab,22} = \int_{\Omega^e} \lambda N_{a,2}N_{b,2} d\Omega, \tag{A18}$$

$$\bar{\bar{k}}_{ab,23} = \int_{\Omega^e} \lambda\psi N_{a,2} N_b d\Omega, \tag{A19}$$

$$\bar{\bar{k}}_{ab,31} = \int_{\Omega^e} \lambda\psi N_a N_{b,1} d\Omega, \tag{A20}$$

$$\bar{\bar{k}}_{ab,32} = \int_{\Omega^e} \lambda\psi N_a N_{b,2} d\Omega, \tag{A21}$$

$$\bar{\bar{k}}_{ab,33} = \int_{\Omega^e} \lambda\psi^2 N_a N_b d\Omega, \tag{A22}$$

where N_a is an element shape function and Ω^e is the domain of the eth element. Element force vectors are calculated as

$$\mathbf{f}^e = \int_{\Omega^e} N_a \mathbf{f}_i d\Omega + \int_{\Gamma^e_h} N_a h_i d\Gamma - \sum_{q \in \eta_g} k^e_{pq} g^e_q, \tag{A23}$$

where $\mathbf{f}_i$ is an element body force vector, $(0, Ra\theta, 0)$, h_i is a traction boundary condition specified at Γ^e_h, and g^e_q is a velocity boundary condition.

APPENDIX B: FINITE-ELEMENT FORMULATION FOR THE 3-D SINGLE-MODE ENERGY EQUATION

Treating basic-field temperature, T, and deviation temperature, θ, collectively as a 2-D vector field, $\mathbf{d}$, the Galerkin formulation of 3-D single-mode energy conservation eqs (32) and (33) may be expressed as

$$\mathbf{M}\dot{\mathbf{d}} + \mathbf{Kd} + \mathbf{F} = 0, \tag{B1}$$

where $\mathbf{M}$, $\mathbf{K}$ and $\mathbf{F}$ are the capacity matrix, the stiffness matrix and the force vector. As in Appendix A, they are constructed using element matrices and vectors. Element capacity matrices, $\mathbf{m}^e$, have dimensions $2n_{\mathrm{en}} \times 2n_{\mathrm{en}}$, and they may be expressed as

$$m^e_{pq} = \mathbf{e}_i^{\mathrm{T}} m^e_{ab} \mathbf{e}_j, \tag{B2}$$

where

$$m^e_{ab,11} = \int_{\Omega^e} (N_a + p) N_b d\Omega, \; m^e_{ab,22} = \int_{\Omega^e} N_a N_b d\Omega, \tag{B3}$$

with zero off-diagonal components. p is the stream-line Petrov–Galerkin shape function defined as in Brooks & Hughes (1982),

$$p = \kappa_{\mathrm{ad}}(UN_{a,1} + WN_{a,2}), \tag{B4}$$

where κ_{ad} is artificial diffusion determined by the basic-field velocity field. Similarly, element stiffness matrices may be

expressed using nodal submatrices as

$$k^e_{pq} = \mathbf{e}_i^{\mathrm{T}} k^e_{ab} \mathbf{e}_j \,, \tag{B5}$$

and

$$k_{ab,11} = \int_{\Omega^e} [(N_a + p)(UN_{b,1} + WN_{b,2}) + N_{a,1}N_{b,1} + N_{a,2}N_{b,2}] d\Omega \,, \tag{B6}$$

$$k_{ab,12} = \frac{1}{2} \int_{\Omega^e} N_a (u_1 N_{b,1} + w_1 N_{b,2} - \psi v_1 N_b) d\Omega \,, \tag{B7}$$

$$k_{ab,21} = \int_{\Omega^e} N_a (u_1 N_{b,1} + w_1 N_{b,2}) d\Omega \,, \tag{B8}$$

$$k_{ab,22} = \int_{\Omega^e} [(N_a + p)(UN_{b,1} + WN_{b,2}) + N_{a,1}N_{b,1} + N_{a,2}N_{b,2} + \psi^2 N_a N_b] d\Omega \,. \tag{B9}$$

Note that we only have to apply the Petrov–Galerkin method to the basic-field temperature, because the single-mode deviation velocity does not cause artificial oscillations in the thermal advection. Element force vectors are calculated from temperature boundary conditions, g^e_q, and heat flux boundary conditions, h_i, as

$$\mathbf{f}^e_p = \sum_{q \in \eta_g} k^e_{pq} g_q - \int_{\Gamma^e_h} N_a h_i d\Gamma \,. \tag{B10}$$